Hankel Dynamic Mode Decomposition for Radar-Based Respiratory Sensing and Tracking

M Gopal Krishna*
Delhi Technological University
mgopalkrishna0007@gmail.com

Suhani Grover*
Delhi Technological University
suhani1077@gmail.com

Chhavi Dhiman
Delhi Technological University
chhavi.dhiman@dtu.ac.in

Abstract

Non-contact respiratory monitoring in uncontrolled environments is a critical unmet need for applications ranging from remote healthcare to search and rescue. While low-power radar is a promising sensing modality, its effectiveness is severely limited by environmental clutter and signal non-stationarity, which cause traditional signal processing pipelines to fail. We present a novel framework for respiratory sensing and tracking that overcomes these limitations by leveraging Hankel Dynamic Mode Decomposition (HDMD) with temporal tracking. Our approach treats the noisy time-series data as the output of a dynamical system and decomposes it into a set of coherent oscillatory modes, enabling the robust isolation of the respiratory signal without requiring extensive hyperparameter tuning. We evaluate our method on a dataset of 24 subjects recorded with a compact pulsed radar in diverse indoor and outdoor conditions. The proposed HDMD pipeline significantly outperforms established decomposition baselines, achieving an NRMSE of 6.00% indoors and 1.33% outdoors, substantially reducing the Root Mean Square Error (RMSE) compared to next-best methods. These results establish HDMD as the first modal decomposition method to extend radar-based respiratory rate estimation and variability analysis into outdoor, mobile contexts, advancing the feasibility of privacy-preserving and low-power physiological sensing. Our code and dataset are available at: https://github.com/Suhani92/HDMD-Respiratory-Rate

1 Introduction

Contactless respiratory monitoring is critical for applications ranging from clinical care to emergency response. Contact-based sensors such as belts or fingertip photoplethysmography (PPG) probes are effective in controlled settings, but they are impractical or unsafe in scenarios like neonatal care, burn treatment, or disaster triage [1–3]. While non-contact imaging PPG using cameras has been explored, it inherits the same limitations as vision-based methods, line of sight, lighting dependence, and privacy concerns [4]. This has driven increasing interest in non-contact sensing to unobtrusively track respiration. Among available modalities, radar [5, 6] has emerged as a particularly promising modality: privacy preservation through motion-only sensing [7], wall-penetration capability, lighting independence, and deployment on compact, low-power platforms.

Despite these advantages, the widespread adoption of these systems is hindered by a performance gap between controlled indoor environments and challenging real-world settings. The fundamen-

*Authors have contributed equally.

39th Conference on Neural Information Processing Systems (NeurIPS 2025) Workshop: Learning to Sense.

tal challenge lies in extracting subtle respiratory motion from signals corrupted by environmental interference, subject movement, and low signal-to-noise ratios in realistic conditions. Traditional spectral analysis methods such as FFT or STFT assume stationarity and thus fail under these conditions [8, 9]. More recent decomposition techniques like Ensemble Empirical Mode Decomposition (EEMD)[10, 11] and Variational Mode Decomposition (VMD)[12, 13] suffer from mode mixing, parameter sensitivity, and computational complexity, rendering them unsuitable for robust, real-time mobile deployment.

In this work, we address this gap by introducing a task-driven framework that jointly considers signal acquisition and analysis. We propose Hankel Dynamic Mode Decomposition (HDMD) with temporal tracking (DMD-t) to decompose noisy radar signals into constituent oscillatory components such as breathing, heartbeat and environmental noise, enabling robust respiratory mode isolation. While DMD and its extensions have found wide applications in fields such as fluid dynamics [14], structural health monitoring[15], and neural signal analysis[16], their use in physiological monitoring remains relatively unexplored. To our knowledge, no prior work has applied HDMD with temporal tracking for respiratory rate extraction, particularly in outdoor environments. This work bridges that gap by extending these methods to robust vital sign monitoring.

Contributions. Our primary contributions are: (1) a framework combining task-specific phase extraction with Hankel-embedded Dynamic Mode Decomposition for respiratory monitoring on low-cost mmWave radar; (2) the first application of a Hankel-DMD pipeline with temporal tracking to isolate quasi-periodic physiological signals from non-stationary outdoor noise; (3) analysis of reconstruction quality characteristics relevant for clinical use cases requiring reliable respiratory waveform extraction; and (4) comprehensive evaluation on 24 subjects showing superior performance with RMSE of 1.14 BPM (6% NRMSE) indoors and 0.4 BPM (1.33% NRMSE) outdoors.

2 Preliminaries

2.1 Signal Model

The radar sensor generates time-series of complex-valued measurements organized as In-phase and Quadrature (IQ) data. For a system with S temporal sweeps and D spatial range bins, the raw measurements are represented as $x[s, d] = I[s, d] + jQ[s, d]$, where $s \in \{1, \ldots, S\}$ denotes the sweeps index and $d \in \{1, \ldots, D\}$ represents the range index. Each complex measurement encodes two essential signal components: the magnitude $|x[s, d]| = \sqrt{I[s, d]^2 + Q[s, d]^2}$, which indicates target presence and location, and the phase $\angle x[s, d] = \arctan(Q[s, d]/I[s, d])$, which captures minute displacements that encode respiratory motion. Detailed explanations of the radar principles and data structure are provided in Appendix B.1 and Appendix B.2.

2.2 Target Detection

The first stage in processing raw radar data is to localize the subject by analyzing the signal's magnitude across all range bins, corresponding to the range-profile and range-slowtime stage in Fig. 1 (steps 1-2). The range bin corresponding to the subject is the one with maximum magnitude, indicating the strongest reflection:

$$d' = \arg\max_{d} \left(\frac{1}{S} \sum_{s=1}^{S} |x[s, d]| \right) \tag{1}$$

To isolate the subject signal and mitigate background clutter, we apply amplitude thresholding and define a spatial window $\{d' - \Delta, \ldots, d' + \Delta\}$ around the detected peak, where Δ corresponds to ± 5 cm. All subsequent processing operates exclusively on IQ data within this window (detailed in Appendix B.2).

2.3 Phase Extraction

While respiratory motion is encoded in the phase variation across sweeps, directly using the arctangent-derived phase [17, 18] is challenging due to phase wrapping within $[-\pi, \pi]$. These discontinuities do not represent actual motion and require separate, often unreliable, unwrapping steps. Instead,

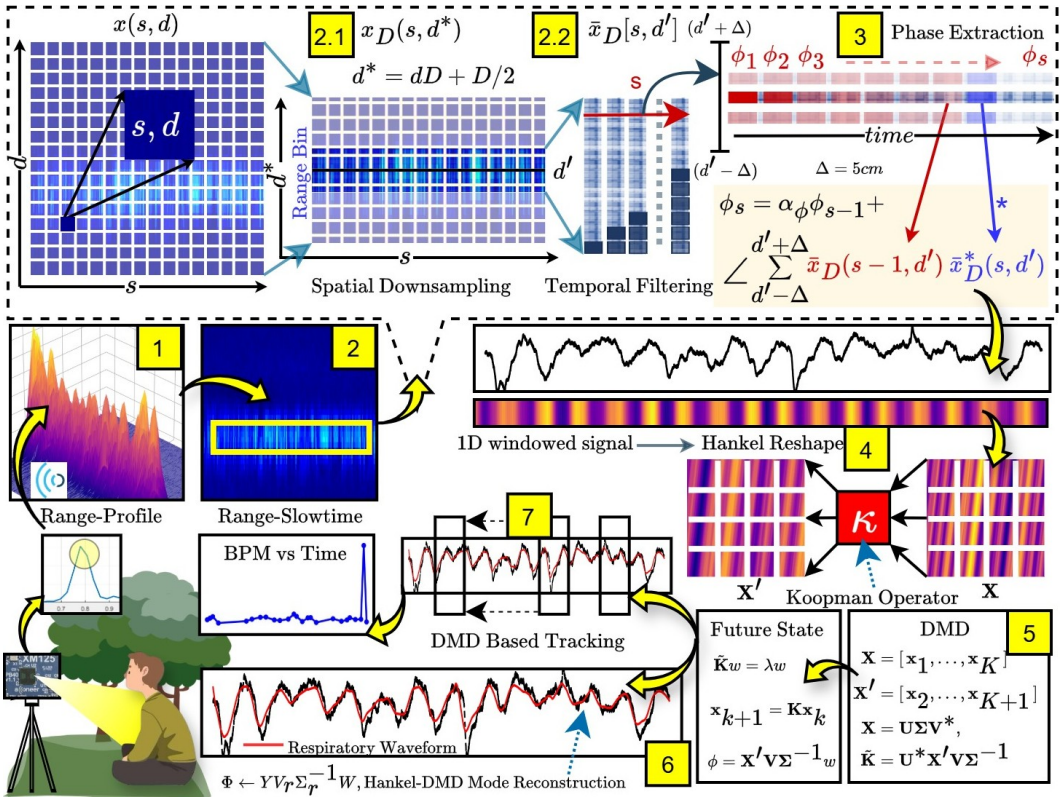

Figure 1: Overview of the HDMD pipeline for respiratory and vital sign tracking using DMD-t. Steps: (1–2) target detection and thresholding to form the range–slowtime matrix and IQ signal $x(s,d)$, (2.1) spatial downsampling, (2.2) temporal filtering, (3) continuous phase extraction, (4) Hankel reshaping, (5) HDMD decomposition, (6) respiratory reconstruction, and (7) DMD-based motion tracking.

we adopt a variation trend method [19] that computes a continuous phase by tracking cumulative displacement over time, as illustrated in Fig. 1 (steps 2.1–3). The IQ signal $x[s,d]$ is first spatially downsampled to $x_D[s,d^*]$ (step 2.1), then temporally low-pass filtered to $\bar{x}_d[s,d^*]$ (step 2.2) to retain respiratory components. The continuous phase is extracted iteratively using a smoothing factor α_ϕ and phase difference obtained by complex conjugation (step 3):

$$\phi[s] = \alpha_\phi \phi[s-1] + \angle \left\{ \sum_{d'=d'-\Delta}^{d'+\Delta} \bar{x}_D[s,d']\,\bar{x}_D^*[s-1,d'] \right\} \tag{2}$$

where $\bar{x}[s,d]$ denotes the filtered IQ data, Δ defines the spatial window around the target, and * represents complex conjugation. The coefficient $\alpha_\phi = \exp(-2f_{\text{low}}/f_s)$ acts as a high-pass filter to suppress low-frequency drift.The resulting continuous phase serves as input to the HDMD-based decomposition for respiratory rate estimation. A detailed derivation is provided in Appendix B.3.

3 Methodology

In this work, we employ Hankel Dynamic Mode Decomposition (HDMD)[20] for respiratory signal analysis, incorporating Hankel matrix embedding, modal decomposition, signal reconstruction, and DMD-t tracking approaches. The pipeline visualized in Fig. 1, spans subject localization (steps 1-2.1), phase extraction (steps 2.2-3), Hankel embedding and Koopman approximation (steps 4-5), signal reconstruction using DMD (step 6), and DMD-t based tracking (step 7).

3.1 Hankel Matrix

The Hankel matrix uses a sliding window to embed the signal into a higher-dimensional space, allowing Dynamic Mode Decomposition to better identify system dynamics. Consider a discrete-time phase signal $\phi = [\phi_1, \phi_2, \ldots, \phi_N]$ sampled at interval Δt. We construct overlapping time-delay embeddings of length m to generate n temporal windows such that $m + n - 1 = N$. The resulting Hankel matrices $\mathbf{X}$ and $\mathbf{Y}$ represent sequential, time-shifted views of the signal and are used to capture temporal evolution for Koopman-based analysis (Fig. 1 steps 4- 5). The Koopman operator approximates the nonlinear evolution of the system via a linear transformation, expressed as

$$\mathbf{Y} \approx \mathbf{K}\mathbf{X} \tag{3}$$

where $\mathbf{K}$ represents the Koopman matrix that captures the system's linearized dynamics in the higher-dimensional embedding space. This pseudo-spatiotemporal embedding improves frequency resolution and enables effective modal decomposition through DMD [21]. To ensure adequate frequency resolution and statistical accuracy across samples, the window length m must satisfy $m \geq \frac{f_s}{f_{\min}}$, where $f_{\min}$ is the lowest frequency of interest [21] with Hankel construction $\mathbf{H} = \text{hankel}(\phi[1:n], \phi[n:N])$ enabling DMD analysis by expressing the physiological signal in multivariate format suitable for modal decomposition.

3.2 Dynamic Mode Decomposition

DMD extracts coherent spatio-temporal modes from high-dimensional time-series data based on Koopman operator theory [21], decomposing data into modes with characteristic frequencies and growth/decay rates by finding the best-fit linear operator $\mathbf{K}$. The eigenvalues of $\mathbf{K}$ capture temporal dynamics, while its eigenvectors define spatial modes, which provide a linear framework for analyzing nonlinear systems. For systems with memory effects, the time series is reshaped into a Hankel matrix of time-delayed embeddings, enabling Hankel-based DMD to identify local Koopman modes and analyze evolving dynamics in nonlinear systems [22]. Assuming a linear transformation between consecutive signal vectors:

$$\mathbf{x}_{k+1} = \mathbf{K}\mathbf{x}_k \tag{4}$$

where $\mathbf{K}$ represents the Koopman operator containing respiratory signal dynamics. The data matrix $\mathbf{X}$ undergoes SVD as:

$$\mathbf{X} = \mathbf{U}\mathbf{\Sigma}\mathbf{V}^*, \quad \mathbf{X}^\dagger = \mathbf{V}\mathbf{\Sigma}^{-1}\mathbf{U}^* \tag{5}$$

where $\mathbf{U} \in \mathbb{C}^{m\times r}$ and $\mathbf{V} \in \mathbb{C}^{n\times r}$ contain the first r left and right singular vectors, $\mathbf{\Sigma} \in \mathbb{R}^{r\times r}$ is the diagonal matrix of the dominant singular values, and the superscript * denotes Hermitian transpose. Projecting $\mathbf{K}$ onto the first r principal components yields the reduced matrix $\tilde{\mathbf{K}} = \mathbf{U}^*\mathbf{Y}\mathbf{V}\mathbf{\Sigma}^{-1}$, and its i-th eigenvalue satisfies $\tilde{\mathbf{K}}\mathbf{w}_i = \lambda_i\mathbf{w}_i$, where $\mathbf{w}_i$ is the i-th eigenvector and λ_i the corresponding eigenvalue.

Spatial modes are recovered as $\boldsymbol{\phi}_i = \mathbf{Y}\mathbf{V}\mathbf{\Sigma}^{-1}\mathbf{w}_i$, where the reduced matrix relates to its eigen decomposition as $\Lambda = \Phi^*\tilde{\mathbf{K}}\Phi$ with $\Lambda = \text{diag}(\mu_1, \mu_2, \ldots, \mu_\kappa)$ and $\Phi = [\phi_1, \phi_2, \ldots, \phi_\kappa]$ denoting the DMD modes.

Applying a modal coordinate transformation $\mathbf{x}_j = \mathbf{\Phi}\mathbf{q}_j$, with $\mathbf{\Phi} = [\boldsymbol{\phi}_1, \boldsymbol{\phi}_2, \ldots, \boldsymbol{\phi}_r]$ and $\mathbf{q}_j$ as modal coordinates at time t_j, we get $q_{j+1} = \Phi^{-1}\mathbf{K}\Phi q_j = \Lambda q_j$. Iterating from $j = 0$ to $j = l$ yields $q_l = \Lambda^l q_0$, with $q_0 = \Phi^{-1}x_0$. Thus, the reconstructed state vector at time l becomes $x_l = \Phi\Lambda^l q_0$, or equivalently $x_l = \sum_{i=1}^{\kappa} \mu_i^l \phi_i q_{0,i}$, where $q_{0,i}$ is the i-th component of q_0.

The conversion of discrete eigenvalues to continuous values s_i [21] is given at a discrete time $\kappa\Delta t$ with $x(0)$ as the initial condition: where s_i captures the temporal characteristics ϕ_i, expressed in terms of natural frequency and damping ratio (see step 6 in Fig. 1).

3.3 Signal Reconstruction & Analysis

We simulate a synthetic breathing signal $\phi(t)$ shown in Fig. 2 (a) with breathing term $f_b(t) = \big(5 + 0.2\sin(2\pi\cdot 0.02t)\big)\cos\Big(\frac{2\pi}{f_s}\sum_{i=1}^{t} f_1(i)\Big)$ using time-varying frequency $f_1(t) = 0.25 + 0.083\sin(2\pi\cdot 0.005t)$ (0.2–0.333 Hz sweep with amplitude modulation), heartbeat component $f_h(t) = \cos(2\pi\cdot 1.2t)$, flutter $f_n(t) = 0.005\cos(2\pi\cdot 5t)$, and scaled Gaussian noise $k\cdot n(t)$:

$$\phi(t) = f_b(t) + f_h(t) + f_n(t) + k\cdot n(t) \tag{6}$$

Respiratory mode isolation is performed using Hankel reshape parameters `N = len(phi)` for total samples and `m = 500` for embedding dimension in longer signals. HDMD achieves consistent reconstruction quality across varying sampling conditions, as shown in Fig. 2 (b). At higher sampling rates, HDMD preserves signal fidelity through adequate embedding, while at lower rates it isolates dominant respiratory modes from eigenmode decomposition, producing smooth frequency variations and amplitude modulations. However, being an inherently data-driven approach, HDMD performance degrades under data sparsity conditions due to insufficient information for optimal Hankel matrix construction and eigenvalue decomposition.

In contrast, Ensemble Empirical Mode Decomposition (EEMD) in Fig. 2 (c) reconstructs respiration from IMFs (bands 5-7) that exhibit inconsistent periodicity and mode mixing. In Fig. 2 (d), Variational Mode Decomposition (VMD), applied with `K=6`, reconstructs breathing mainly from modes 3-5 with moderate waveform fidelity, yet remains sensitive to parameter tuning, offers limited denoising, consistent amplitude mismatch, and requires post-processing to suppress high-frequency flutter. Wavelet decomposition with Daubechies-4 (`db4`) at `max_level=10` in Fig. 2 (e) produces less noisy outputs than VMD but introduces irregularities in feature extraction due to harmonics and cannot match HDMD's smooth amplitude-frequency reconstruction. Amplitude and frequency mismatch can be observed in the 20-60s interval. Evaluating across varying sampling points, Gaussian noise factors, and signal length establishes HDMD as a superior data-driven method for accurate respiratory amplitude extraction, essential for respiratory distress analysis and subsequent classification tasks.

3.4 DMD-t Tracking

Standard Fourier Analysis (STFT) is unable to capture the non-stationary and time-varying respiratory signal. DMD-based tracking (DMD-t)[23] addresses this limitation by iterative decomposition within overlapping windows to track evolving dynamics in the signal (Fig. 1, step 7). For each window i centered at $t^{(i)}$, the Koopman approximation yields eigen values ($\lambda_j^{(i)}$) that represent local signal dynamics. Sliding window maps the time-frequency evolution of the extracted mode and the `window_size` and `step_size` balance the temporal resolution. The overall algorithmic pipeline is briefly discussed in Fig. 9, with implementation details on phase data is provided in Appendix C.1.

4 Experiments and Results

4.1 Dataset Acquisition and Experimental Setup

We evaluate our approach on both synthetic breathing signals and real-time captured radar signals. For real data, we use a self-collected dataset from 24 participants (12 male, 12 female, aged 20-60) recorded with low-cost 60.5 GHz pulsed coherent mmWave radar across three postures (sitting, standing, lying) and two environments (indoor and outdoor). The outdoor experiments were conducted in uncontrolled environments with clutter and interference, providing a challenging testbed for sensor algorithm robustness.

Ground truth measurements were obtained using synchronized clinical-grade capnography and pulse oximeter devices for indoor scenarios (Figure 3d-e), while outdoor measurements relied on portable pulse oximetry due to equipment mobility constraints (Figure 13). Cross-validation between the two reference devices on indoor data shows RMSE of 0.74 BPM (3.87% NRMSE), indicating that the portable oximeter provides sufficiently reliable ground truth within its rated ±1 BPM accuracy.

Additionally, to optimize signal acquisition, we conducted a comparative testing of three antenna configurations: radar module without lens, plano-convex dielectric lens, and Fresnel Zone Plate (FZP) lens. Based on our evaluation across all subjects (detailed results in Table 3), the plano-convex lens from Acconeer's lens kit achieved optimal performance with RMSE of 0.89 compared to 1.15 for FZP and 1.88 for no-lens configurations. The lens focuses the radar beam on the subject's chest region while suppressing environmental reflections, significantly improving signal-to-noise ratio at typical monitoring distances of 1.5-2m (Figure 3). Comprehensive analysis of lens selection, including its effect on extracted phase and estimated respiratory rate, along with complete hardware specifications and data acquisition details, is provided in Appendix D.

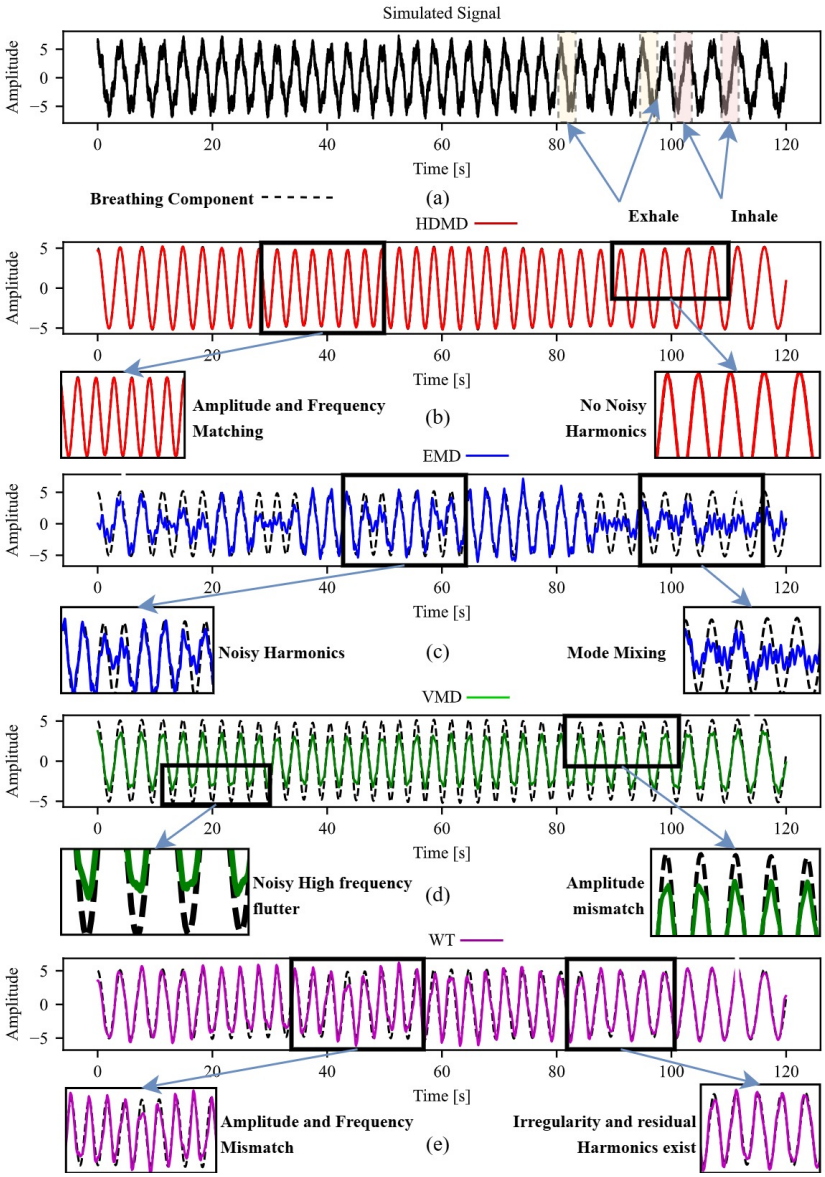

Figure 2: Reconstruction of a synthetically generated physiological signal. (a) Ground truth signal; (b–e) reconstructions using HDMD, EEMD, VMD, and DWT, respectively. Each method extracts the underlying respiratory carrier from the noisy input, with reconstruction errors and mismatches highlighted in the marked time segments.

4.2 Baselines and Metrics

Baselines: We compare HDMD with the following methods: (a) Variational Mode Decomposition (VMD), (b) Wavelet Transform (DWT), (c) Ensemble Empirical Mode Decomposition (EEMD), (d) Compressed Sensing with Orthogonal Matching Pursuit (CS-OMP), (e) Wavelet Cosine Transform (WCT), (f) Band-Pass Filtering (BPF), (g) Moving Average (MAV), and (h) Finite Impulse Response (FIR) filtering (see Appendix E.1 for detailed formulations).

Metrics: We employ Pearson Correlation Coefficient (PCC) to assess waveform similarity preservation, Mean Squared Error (MSE) for reconstruction fidelity, Root Mean Squared Error (RMSE) and Normalized RMSE (NRMSE) for respiratory rate estimation accuracy (detailed definitions are in Appendix E.2).

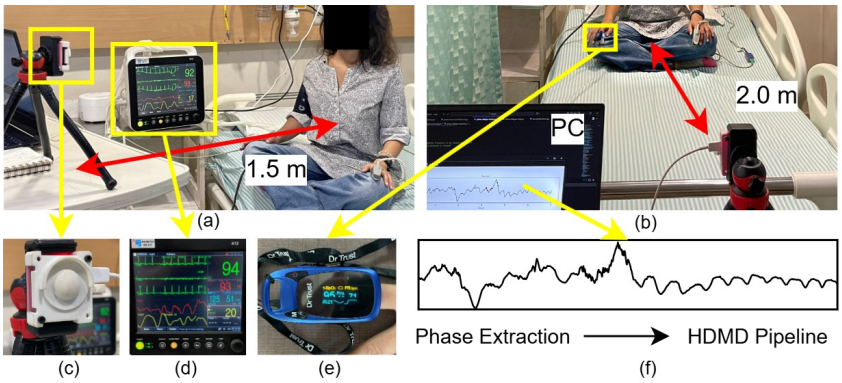

Figure 3: Experimental setup for radar-based respiratory monitoring. (a) Indoor data collection with subject at 1.5m distance; (b) Data collection at 2.0m distance; (c) Acconeer XM125 radar module with plano-convex lens; (d) Clinical-grade capnography reference device; (e) Portable pulse oximeter reference device; (f) Extracted phase signal.

Table 1: Performance comparison across varying parameters

Method	**Sampling Frequency** (f_s)				**Gaussian Noise Factor** (k)				**Signal Duration** (t)			
	$f_s = 240$Hz		$f_s = 100$Hz		$k = 0.5$		$k = 3$		$t = 120s$		$t = 180s$	
	MSE	**PCC**	**MSE**	**PCC**	**MSE**	**PCC**	**MSE**	**PCC**	**MSE**	**PCC**	**MSE**	**PCC**
HDMD	**0.16**	**0.994**	**1.26**	0.958	**0.006**	**1.000**	**0.54**	**0.985**	**0.54**	**0.985**	0.64	0.980
EEMD	2.42	0.899	1.37	0.952	3.64	0.801	4.68	0.731	1.68	0.931	3.92	0.830
VMD	1.85	0.993	3.62	**0.989**	0.93	0.993	1.72	0.983	0.92	0.983	0.73	**0.983**
DWT	1.15	0.953	2.56	0.892	0.76	0.969	0.80	0.958	0.79	0.968	**0.63**	0.975

4.3 Ablation Study

We conduct systematic ablation studies to analyze HDMD performance across sampling frequency (f_s), signal duration (t), and Gaussian noise factor (k), with quantitative results summarized in Table 1. An extended analysis is available in Appendix F.1.

Sampling Frequency (f_s): Table 1 presents the effect of reducing f_s from 240 Hz to 100 Hz. HDMD achieves the best performance at high sampling (0.16 MSE, 0.994 PCC), but reconstruction errors increase when the data becomes sparse (1.26 MSE, 0.958 PCC). VMD maintains high correlation (0.993 $\rightarrow$ 0.989) but with larger MSE (1.85 $\rightarrow$ 3.62), while DWT and especially EEMD degrade more severely. These results confirm HDMD's dependence on adequate data density due to its data-driven nature.

Gaussian Noise Factor (k): To assess robustness under outdoor conditions, we vary k between 0.5 and 3. As shown in Table 1, HDMD remains stable, achieving near-perfect reconstruction at low noise levels ($k = 0.5$:0.006 MSE, 1.000 PCC) and maintaining high accuracy even under elevated noise ($k = 3$:0.54 MSE, 0.985 PCC). In contrast, EEMD exhibits counterintuitive behavior where moderate noise appears to aid decomposition (increased MSE 4.64, reduced PCC 0.731).VMD maintains stability across noise levels (0.993 $\rightarrow$ 0.983 PCC with slight MSE increase), while DWT shows consistent robustness (0.969 $\rightarrow$ 0.958 PCC). This demonstrates HDMD's resilience to harmonics and flutter under noisy conditions while revealing that certain decomposition methods can even benefit from controlled noise injection.

Signal Duration (t): Increasing signal length improves embedding richness for Hankel construction. Table 1 shows that HDMD sustains competitive accuracy at both durations (120 s: 0.54 MSE, 0.985 PCC; 180 s: 0.64 MSE, 0.980 PCC). At 180s, DWT achieves the lowest MSE (0.63) but with reduced correlation (0.975), while VMD achieves a higher correlation (0.983) and higher MSE (0.73). EEMD shows the most significant degradation with longer signals (MSE increases from 1.68 to 3.92). Setting $m \geq f_s/f_{\min}$ improves frequency resolution for sparse data and ensures stable reconstruction.

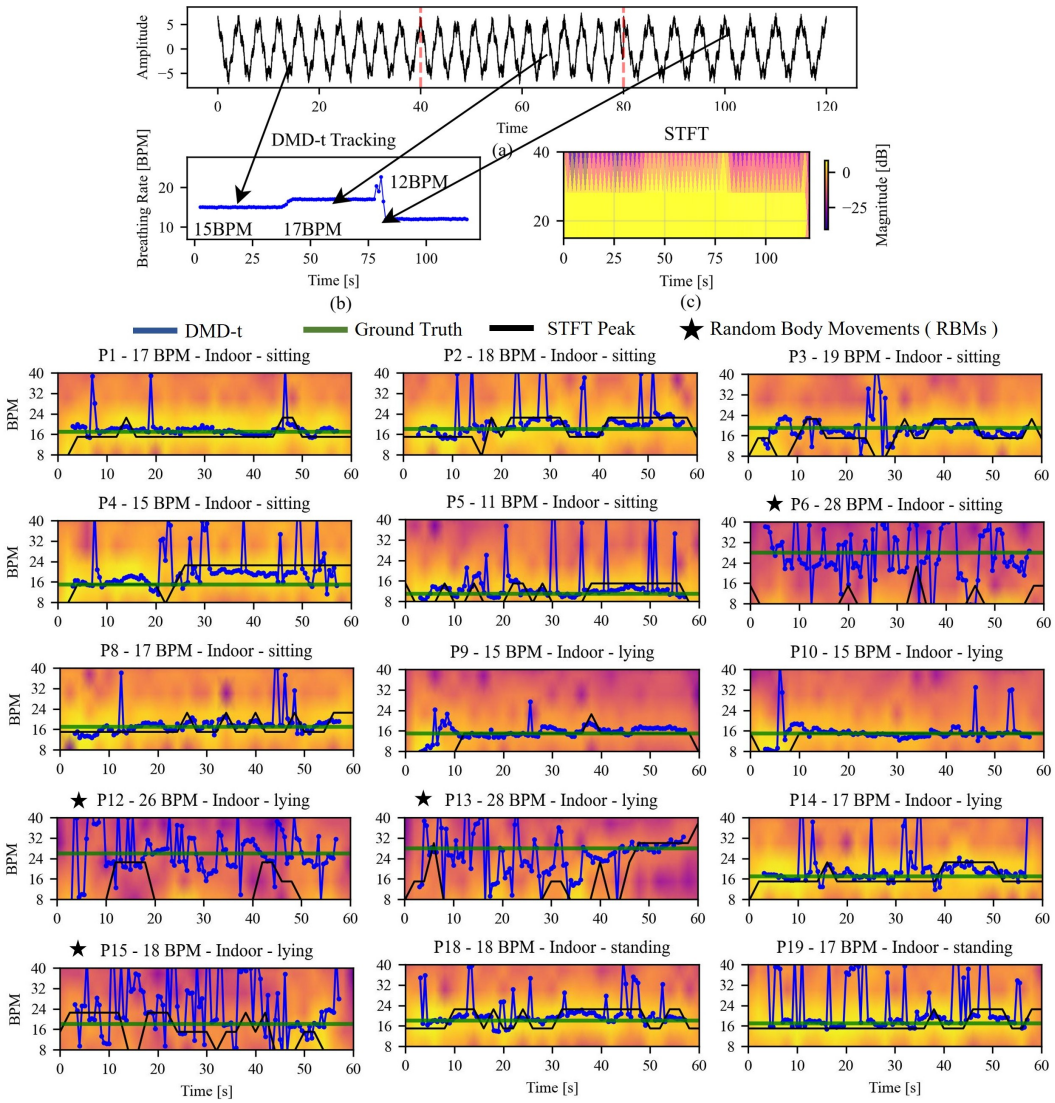

Figure 4: DMD-t respiratory tracking where each subplot shows the instantaneous respiratory rate over the DMD-t spectrogram, where color intensity indicates spectral energy concentration. P6, P12, P13, P15, and P24 show random body movements (RBMs), while others exhibit stable breathing cycles. (a) Original signal with time-varying breathing rates; (b) DMD-t tracking results; (c) STFT spectrogram exhibits spectral leakage and reduced interpretability.

4.4 DMD-t Tracking Performance

For tracking evaluation, we construct a synthetic 120-s breathing signal sampled at 300 Hz with a time-varying respiratory component, heartbeat interference, high-frequency flutter, and additive Gaussian noise shown in Fig. 4 (a). The benchmark signal is defined in Eq. (7):

$$f_b(t) = \begin{cases} [5 + 0.2\sin(2\pi \cdot 0.02t)]\sin(2\pi \cdot 0.25t), & 0 \le t < 40 \\ [5 + 0.3\sin(2\pi \cdot 0.015t)]\sin(2\pi \cdot 0.283t), & 40 \le t < 80 \\ [5 + 0.15\sin(2\pi \cdot 0.025t)]\sin(2\pi \cdot 0.2t), & 80 \le t \le 120 \end{cases} \tag{7}$$

with respiratory rates of 0.25, 0.283, and 0.2 Hz (15, 17, 12 BPM), heartbeat interference $f_h(t) = A_h \sin(2\pi \cdot 1.2t)$, flutter $f_n(t) = A_n \sin(2\pi \cdot 5t)$, and variable Gaussian noise $k \cdot n(t)$ for performance evaluation. As shown in Fig. 4 (b), DMD-t demonstrates superior tracking as compared to STFT Fig. 4 (c), particularly during rapid transitions with improved resolution and reduced spectral leakage.

Table 2: Respiratory rate measurements (BPM) comparing HDMD against baseline methods across 24 participants in six scenarios (indoor/outdoor × sitting/lying/standing). Ground truth from capnography (indoor) and oximeter (outdoor). RBM denotes random body movements.

Person ID	Ground Truth (BPM)		Measured Rate (BPM)								
	Capnography	Oximeter	HDMD	VMD	DWT	EEMD	CS-OMP	WCT	BPF	MAV	FIR
Indoor - Sitting											
P1	17	17	**17.2**	17.7	18	18	19	30	28	26	25
P2	18	18	18.2	18.8	19	**18**	4	5	7	8	9
P3	19	18	19.01	18.89	**19**	18	22	32	30	28	27
P4	15	16	**16.34**	19.5	20	20	32	30	28	25	24
P5	11	12	**11.15**	11.51	12	12	26	24	22	20	18
P6 (RBM)	28	28	**27.4**	10.23	3	14	10	12	14	16	18
P7	9	9	**8.12**	7.75	8	8	25	23	21	19	18
P8	17	17	**16.62**	18.2	18	18	12	3	5	7	8
Indoor - Lying											
P9	15	16	11.31	**15.32**	16	16	33	31	29	26	24
P10	15	16	12.84	14.74	**15**	16	2	1	3	5	6
P11	10	11	**10.5**	11.67	16	16	28	26	24	21	20
P12 (RBM)	26	26	27.02	9.73	3	**26**	8	10	12	15	16
P13 (RBM)	28	29	**29.23**	12.25	3	14	9	11	13	16	18
P14	17	18	**17.68**	17.99	18	18	36	34	32	29	27
P15 (RBM)	18	18	**18.62**	13.57	4	12	2	4	2	4	6
P16	18	18	18.05	18.01	**18**	**18**	38	36	34	31	29
Indoor - Standing											
P17	19	18	**18.02**	17.08	17	18	1	3	5	8	10
P18	18	19	**18.37**	19.3	19	20	39	37	35	32	30
P19	17	16	17.14	17.41	**17**	16	3	1	3	6	8
P20	20	20	**20.88**	18.85	19	18	15	3	5	8	10
P21	19	19	19.23	18.93	**19**	20	42	40	38	35	33
P22	18	18	18.02	18.99	19	**18**	2	4	6	3	5
P23	19	18	**19.64**	16.91	18	18	17	41	39	36	34
P24 (RBM)	22	21	**23.9**	18.98	19	18	17	3	5	8	10
Performance Metrics											
RMSE		0.74	**1.14**	6.12	9.27	4.68	17.81	16.14	14.33	11.99	10.34
NRMSE (%)		3.90	**6.00**	32.20	48.80	24.60	93.70	85.00	75.40	63.10	54.40
Outdoor - Sitting											
P1	–	9	**9.03**	9.75	10	10	10	8	5	19	4
P2	–	11	**11.2**	13.39	13	14	11	31	2	18	22
P3	–	20	**19.7**	18.91	19	18	17	4	7	9	7
P4 (RBM)	–	18	**17.59**	7.86	6	14	13	5	12	11	28
P5	–	16	**15.9**	14.7	15	14	2	15	29	15	7
P6	–	14	14.42	14.2	15	**14**	12	8	3	11	12
P7	–	13	**13.71**	14.3	14	14	12	3	2	12	3
P8	–	21	**21.13**	19.89	3	20	5	20	5	17	33
Outdoor - Lying											
P9	–	16	**15.67**	14.12	13.8	14.3	19	25	2	12	12
P10	–	13	**12.82**	11.95	12	12	4	8	39	33	2
P11	–	19	18.88	18	**19**	18	10	**19**	21	2	12
P12 (RBM)	–	30	**29.8**	6.96	3	14	10	7	21	2	4
P13	–	25	**25.16**	25.71	26	26	22	5	5	22	12
P14	–	10	9.74	10.76	11	**10**	4	2	24	34	12
P15	–	13	**12.53**	11	12	12	4	21	30	12	9
P16	–	25	**25.92**	27.37	3	26	12	35	3	2	7
Outdoor - Standing											
P17 (RBM)	–	33	**32.72**	9.01	4	32	12	8	22	12	12
P18	–	17	**17.71**	17.91	18	14	12	5	11	14	11
P19	–	15	**15.73**	15.84	14	16	3	16	5	22	10
P20	–	16	**15.75**	11.51	12	12	8	6	32	11	14
P21	–	12	**12.29**	13.96	14	14	18	32	6	17	13
P22	–	39	**39.14**	22.49	3	38	28	5	28	16	12
P23 (RBM)	–	20	**20.3**	8.82	5	16	12	26	34	12	11
P24 (RBM)	–	19	**19.33**	9.01	4	18	21	36	5	2	12
Performance Metrics											
RMSE			**0.4**	8.56	13.40	3.81	9.70	14.40	13.47	13.51	12.05
NRMSE (%)			**1.33**	28.55	44.66	12.71	32.33	48.01	44.91	45.04	40.17

DMD-t achieves superior physical interpretability and resolution as compared to spectrograms, which suffer from fixed windowing constraints and spectral leakage. Real-time phase signal tracking (6-s windows, 0.5-s step) is shown in Fig. 4, with results corresponding to indoor scenarios in Table 2. Ground truth comparisons reveal that DMD-t provides higher resolution even in challenging random body movement (RBM) cases, consistent with HDMD's accuracy. This capability is critical for respiratory variability analysis and distress classification. Additional real-time radar tracking results are provided in the Appendix C.1.

4.5 Results

Table 2 presents respiratory rate estimation results across 24 participants in six experimental scenarios. HDMD achieves superior performance with indoor RMSE of 1.14 (6% NRMSE) and outdoor RMSE of 0.4 (1.33% NRMSE), substantially outperforming all baseline methods.

For indoor scenarios, decomposition methods show competitive performance with EEMD and VMD achieving moderate accuracy (RMSE 4.68 and 6.12 respectively), and outperforming DWT (RMSE 9.27). Among traditional filtering approaches, FIR demonstrates the best baseline performance (RMSE 10.34). For outdoor scenarios, EEMD and VMD perform competitively (RMSE 3.81 and 8.56 respectively), outperforming DWT (RMSE 13.40), while CS-OMP is the strongest traditional method (RMSE 9.70). The lower outdoor error reflects the ±1 BPM accuracy limitation of the portable oximeter compared to medical-grade capnography. Across both settings, HDMD maintains consistent superiority with sub-7% indoor and sub-2% outdoor error rates.

HDMD's performance stems from its ability to effectively isolate respiratory components from environmental interference through Hankel embeddings. Notably, cases marked in Table 2 as RBM (random body movements) demonstrate HDMD's robustness to motion artifacts where decomposition methods like VMD fail dramatically (e.g., P6, P12, P13 with errors exceeding 10+ BPM), HDMD maintains accurate estimation within 1-2 BPM of ground truth. The method achieves consistent sub-7% indoor and sub-2% outdoor error rates across all conditions, including scenarios with body movements and environmental clutter.

5 Discussion and Conclusion

Computational Complexity and Limitations: Runtime evaluation on a 120-second signal (300 Hz) shows HDMD's primary limitation: with an average processing time of 5.4 s, it is approximately 6.3× slower than VMD (0.86 s), and $\sim 1000\times$ slower than DWT (4 ms), though $20\times$ faster than EEMD (38.9 s). As a data-driven method, HDMD requires dense sampling for effective Hankel embeddings, yielding $\mathcal{O}(n^2)$ to $\mathcal{O}(n^3)$ complexity but enabling superior denoising and harmonic suppression, particularly under random body movements where faster methods such as DWT and VMD fail (Table 2). This computational cost currently limits real-time deployment without optimization. Additional limitations include performance degradation under sparse sampling and sensitivity to embedding dimension parameters, though less pronounced than in VMD.

Future Work: Further research directions include: (1) adaptive parameter selection for automated Hankel embedding optimization; (2) extension to multi-person tracking using MIMO radar arrays; (3) integration of motion cancellation algorithms for random body movements; (4) comprehensive vital sign monitoring including heart rate estimation; and (5) deployment on edge computing platforms with optimized waveform reconstruction maintaining high frequency resolution.

Conclusion: We present HDMD as a framework for radar-based respiratory monitoring, achieving superior performance as compared to traditional decomposition methods across diverse environmental conditions. Our approach effectively isolates physiological signals from complex interference through mode decomposition. While computational overhead remains a challenge, HDMD's signal reconstruction and noise resilience establish a strong foundation for contactless physiological monitoring. DMD-t tracking enables non-stationary respiratory analysis, advancing practical deployment of privacy-preserving, low-power vital sign monitoring in clinical and mobile health applications.

References

[1] Mohammed Al-khafajiy, Thar Baker, Carl Chalmers, Muhammad Asim, Hoshang Kolivand, Muhammad Fahim, and Atif Waraich. Remote health monitoring of elderly through wearable sensors. *Multimedia Tools and Applications*, 78:1–26, 09 2019. doi: 10.1007/s11042-018-7134-7.

[2] Robert Steele, Amanda Lo, Chris Secombe, and Yuk Wong. Elderly persons' perception and acceptance of using wireless sensor networks to assist healthcare. *International journal of medical informatics*, 78:788–801, 09 2009. doi: 10.1016/j.ijmedinf.2009.08.001.

[3] Mauricio Villarroel, Sitthichok Chaichulee, Joao Jorge, Sara Davis, Gabrielle Green, Carlos Arteta, Andrew Zisserman, Kenny McCormick, Peter Watkinson, and L. Tarassenko. Non-contact physiological monitoring of preterm infants in the neonatal intensive care unit. *npj Digital Medicine*, 2:128, 12 2019. doi: 10.1038/s41746-019-0199-5.

[4] Lingyun Ren, Lingqin Kong, Farnaz Foroughian, Haofei Wang, Paul Theilmann, and Aly E. Fathy. Comparison study of noncontact vital signs detection using a doppler stepped-frequency continuous-wave radar and camera-based imaging photoplethysmography. *IEEE Transactions on Microwave Theory and Techniques*, 65(9):3519–3529, 2017. doi: 10.1109/TMTT.2017.2658567.

[5] A.G. Yarovoy, L.P. Ligthart, Jonas Matuzas, and Boris Levitas. Uwb radar for human being detection [same as uwb radar for human being detection, ibid., vol. 21, n. 11, 06]. *Aerospace and Electronic Systems Magazine, IEEE*, 23:36 – 40, 06 2008. doi: 10.1109/MAES.2008.4523914.

[6] Laura Anitori, Ardjan Jong, and F. Nennie. Fmcw radar for life-sign detection. pages 1 – 6, 06 2009. doi: 10.1109/RADAR.2009.4976934.

[7] Øyvind Aardal, Yoann Paichard, Sverre Brovoll, Tor Berger, Tor Sverre Lande, and Svein-Erik Hamran. Physical working principles of medical radar. *IEEE Transactions on Biomedical Engineering*, 60(4):1142–1149, 2013. doi: 10.1109/TBME.2012.2228263.

[8] Mohamed Mabrouk, Sreeraman Rajan, Miodrag Bolic, Mohamad Forouzanfar, Hilmi R. Dajani, and Izmail Batkin. Human breathing rate estimation from radar returns using harmonically related filters. *Journal of Sensors*, 2016(1):9891852, 2016. doi: https://doi.org/10.1155/2016/9891852. URL `https://onlinelibrary.wiley.com/doi/abs/10.1155/2016/9891852`.

[9] Zhanjun Hao, Yue Wang, Fenfang Li, Guozhen Ding, Kai Fan, and Yifei Gao. Detection of vital signs based on millimeter wave radar. *Scientific Reports*, 15, 08 2025. doi: 10.1038/s41598-025-09112-w.

[10] Degui Yang, Zhengliang Zhu, and Buge Liang. Vital sign signal extraction method based on permutation entropy and eemd algorithm for ultra-wideband radar. *IEEE Access*, PP:1–1, 12 2019. doi: 10.1109/ACCESS.2019.2958600.

[11] Hongming Shen, Chen Xu, Yongjie Yang, Ling Sun, Zhitian Cai, Lin Bai, Edward Clancy, and Xinming Huang. Respiration and heartbeat rates measurement based on autocorrelation using ir-uwb radar. *IEEE Transactions on Circuits and Systems II: Express Briefs*, PP:1–1, 07 2018. doi: 10.1109/TCSII.2018.2860015.

[12] Konstantin Dragomiretskiy and Dominique Zosso. Variational mode decomposition. *IEEE Transactions on Signal Processing*, 62(3):531–544, 2014. doi: 10.1109/TSP.2013.2288675.

[13] Xiangyu Xu, Jiadi Yu, Chengguang Ma, Yanzhi Ren, Hongbo Liu, Yanmin Zhu, Yi-Chao Chen, and Feilong Tang. mmecg: Monitoring human cardiac cycle in driving environments leveraging millimeter wave. In *IEEE INFOCOM 2022 - IEEE Conference on Computer Communications*, page 90–99. IEEE Press, 2022. doi: 10.1109/INFOCOM48880.2022.9796912. URL `https://doi.org/10.1109/INFOCOM48880.2022.9796912`.

[14] Hiroyuki Asada and Soshi Kawai. Exact parallelized dynamic mode decomposition with hankel matrix for large-scale flow data, 09 2024.

[15] Jae seung Hwang and Hongjin Kim. Mode decomposition of structures with closely distributed modes and nonclassical damping. *Structural Control and Health Monitoring*, 25:e2065, 07 2017. doi: 10.1002/stc.2065.

[16] Bingni W. Brunton, Lise A. Johnson, Jeffrey G. Ojemann, and J. Nathan Kutz. Extracting spatial–temporal coherent patterns in large-scale neural recordings using dynamic mode decomposition. *Journal of Neuroscience Methods*, 258:1–15, January 2016. ISSN 0165-0270. doi: 10.1016/j.jneumeth.2015.10.010. URL http://dx.doi.org/10.1016/j.jneumeth.2015.10.010.

[17] Byung-Kwon Park, Olga Boric-Lubecke, and Victor M. Lubecke. Arctangent demodulation with dc offset compensation in quadrature doppler radar receiver systems. *IEEE Transactions on Microwave Theory and Techniques*, 55(5):1073–1079, 2007. doi: 10.1109/TMTT.2007.895653.

[18] Jingyu Wang, Xiang Wang, Lei Chen, Jiangtao Huangfu, Changzhi Li, and Lixin Ran. Noncontact distance and amplitude-independent vibration measurement based on an extended dacm algorithm. *IEEE Transactions on Instrumentation and Measurement*, 63(1):145–153, 2014. doi: 10.1109/TIM.2013.2277530.

[19] Nima Bahmani, Markku Rouvala, and Arto Kaarna. Vital sign detection using short-range mm-wave pulsed radar. pages 512–516, 03 2021. doi: 10.1109/LifeTech52111.2021.9391910.

[20] Matthew J. Colbrook. The multiverse of dynamic mode decomposition algorithms, 2023. URL https://arxiv.org/abs/2312.00137.

[21] Hassan Arbabi and Igor Mezić. Ergodic theory, dynamic mode decomposition, and computation of spectral properties of the koopman operator. *SIAM Journal on Applied Dynamical Systems*, 16(4):2096–2126, January 2017. ISSN 1536-0040. doi: 10.1137/17m1125236. URL http://dx.doi.org/10.1137/17M1125236.

[22] Gerui Wang, Jiang Wu, Xiaoge Chen, and Yixin Du. A sensor signal processing method based on hankel dynamic mode decomposition. *Measurement Science and Technology*, 36, 02 2025. doi: 10.1088/1361-6501/adb5b0.

[23] Maziar S. Hemati, Matthew O. Williams, and Clarence W. Rowley. Dynamic mode decomposition for large and streaming datasets. *Physics of Fluids*, 26(11), November 2014. ISSN 1089-7666. doi: 10.1063/1.4901016. URL http://dx.doi.org/10.1063/1.4901016.

[24] R. Rox Anderson and John A. Parrish. The optics of human skin. *Journal of Investigative Dermatology*, 77(1):13–19, 1981. ISSN 0022-202X. doi: https://doi.org/10.1111/1523-1747.ep12479191. URL https://www.sciencedirect.com/science/article/pii/S0022202X15461251.

[25] Yunhao Ba, Zhen Wang, Kerim Doruk Karinca, Oyku Deniz Bozkurt, and Achuta Kadambi. Overcoming difficulty in obtaining dark-skinned subjects for remote-ppg by synthetic augmentation, 2021. URL https://arxiv.org/abs/2106.06007.

[26] Vytautas Vizbara. Comparison of green, blue and infrared light in wrist and forehead photoplethysmography. In *BioMed*, 2013. URL https://api.semanticscholar.org/CorpusID:110981655.

[27] Ewa M. Nowara, Daniel McDuff, and Ashok Veeraraghavan. A meta-analysis of the impact of skin tone and gender on non-contact photoplethysmography measurements. In *Proceedings of the IEEE/CVF Conference on Computer Vision and Pattern Recognition (CVPR) Workshops*, June 2020.

[28] Y. Kim, Y. Park, J. Kim, and E.C. Lee. Remote heart rate monitoring method using infrared thermal camera. *International Journal of Engineering Research and Technology*, 11:493–500, 01 2018.

[29] Toshiaki Negishi, Shigeto Abe, Takemi Matsui, He Liu, Masaki Kurosawa, Tetsuo Kirimoto, and Guanghao Sun. Contactless vital signs measurement system using rgb-thermal image sensors and its clinical screening test on patients with seasonal influenza. *Sensors*, 20(8), 2020. ISSN 1424-8220. doi: 10.3390/s20082171. URL https://www.mdpi.com/1424-8220/20/8/2171.

[30] Eric C. Larson, TienJui Lee, Sean Liu, Margaret Rosenfeld, and Shwetak N. Patel. Accurate and privacy preserving cough sensing using a low-cost microphone. In *Proceedings of the 13th International Conference on Ubiquitous Computing*, UbiComp '11, pages 375–384, New York, NY, USA, 2011. ACM. ISBN 978-1-4503-0630-0. doi: 10.1145/2030112.2030163. URL http://doi.acm.org/10.1145/2030112.2030163.

[31] Justice Amoh and Kofi Odame. Deep neural networks for identifying cough sounds. *IEEE Transactions on Biomedical Circuits and Systems*, PP:1–9, 09 2016. doi: 10.1109/TBCAS.2016.2598794.

[32] Sérgio Matos, Surinder Birring, Ian Pavord, and David Evans. Detection of cough signals in continuous audio recordings using hidden markov models. *IEEE transactions on bio-medical engineering*, 53:1078–83, 07 2006. doi: 10.1109/TBME.2006.873548.

[33] DANIEL N. KASLOVSKY and FRANÇOIS G. MEYER. Noise corruption of empirical mode decomposition and its effect on instantaneous frequency. *Advances in Adaptive Data Analysis*, 02(03):373–396, July 2010. ISSN 1793-7175. doi: 10.1142/s1793536910000537. URL http://dx.doi.org/10.1142/S1793536910000537.

[34] Chuchu Liang, Majid Khan, Lili Wu, and Zhixiang Zhang. Ecg signal data classification system based on hankel dynamic mode decomposition. *Malaysian Journal of Fundamental and Applied Sciences*, 21, 02 2025. doi: 10.11113/mjfas.v21n1.3928.

[35] Honorine Niyigena Ingabire, Kangjia Wu, Joan Toluwani Amos, Sixuan He, Xiaohang Peng, Wenan Wang, Min Li, Jinying Chen, Yukun Feng, Nini Rao, and Peng Ren. Analysis of ecg signals by dynamic mode decomposition. *IEEE Journal of Biomedical and Health Informatics*, 26(5):2124–2135, 2022. doi: 10.1109/JBHI.2021.3130275.

[36] Efe Ilicak, Safa Ozdemir, Jascha Zapp, Lothar Schad, and Frank Zöllner. Dynamic mode decomposition of dynamic mri for assessment of pulmonary ventilation and perfusion. *Magnetic Resonance in Medicine*, 90, 03 2023. doi: 10.1002/mrm.29656.

[37] Gyurhan Nedzhibov. Blind source separation using time-delayed dynamic mode decomposition. *Computation*, 13(2), 2025. ISSN 2079-3197. doi: 10.3390/computation13020031. URL https://www.mdpi.com/2079-3197/13/2/31.

A Related Work

Non-Contact Respiratory Monitoring: Camera-based methods [24–27] achieve high accuracy in controlled settings but suffer from lighting dependency, privacy concerns, and computational overhead. RGB photoplethysmography requires stable illumination and line-of-sight, while thermal imaging [28, 29] demands expensive sensors and struggles with ambient heat sources. Audio-based approaches [30–32] using microphones or ultrasonics require close proximity and fail under environmental noise. These constraints severely limit deployment in mobile, outdoor, or privacy-sensitive scenarios where radar's unique advantages including lighting independence, clothing penetration, and compact hardware become critical.

Radar Signal Processing for Vital Signs: Traditional algorithms employ arc-tangent demodulation followed by spectral analysis (FFT, STFT). These frequency-domain methods assume signal stationarity, failing when respiratory patterns exhibit natural amplitude and frequency variations common in real-world conditions. Time-frequency approaches including STFT and wavelets partially address non-stationarity but suffer from fundamental resolution trade-offs that obscure physiological variations [8, 9]. Recent adaptive methods like EEMD and VMD show improvements but exhibit critical limitations: EEMD suffers from mode mixing in noisy conditions [33], while VMD requires careful parameter tuning and struggles with denoising under real-time constraints [13]. Compressive sensing approaches impose sparsity assumptions poorly aligned with oscillatory physiological signals.

Dynamic Mode Decomposition: Originally developed for fluid dynamics, DMD identifies coherent spatiotemporal modes through Koopman operator approximation and has achieved success across structural health monitoring, neuroscience (fMRI/EEG analysis), and biomedical signal processing. Standard DMD requires spatial measurements; Hankel DMD extends to scalar time series through delay embedding, enabling robust mode extraction from single-channel data. Recent work on ECG classification [34–36] demonstrates HDMD's superior performance over standard DMD for unstable physiological modes. Time-resolved variants [37, 23] including sliding-window DMD enable tracking of evolving dynamics, yet applications to radar-based respiratory monitoring remain unexplored.

B Preliminary Methodology

B.1 Fundamentals of Pulsed Coherent Radar

The sensor operates as a pulsed coherent radar in the millimeter-wave spectrum, specifically at a carrier frequency of 60.5 GHz. Its pulsed nature means the radar transmits short-duration wavelets of electromagnetic energy rather than a continuous wave. When these pulses encounter an object, they reflect back to the sensor, enabling the measurement of the time delay (t_{delay}) between transmission and reception. This delay determines the distance (d) to the target, calculated as

$$d = 2 \cdot t_{\text{delay}} \cdot v, \qquad v = \frac{c_0}{\sqrt{\varepsilon_r}} \tag{8}$$

here, v is the wave speed in the medium, c_0 is the speed of light in vacuum, and ε_r is the relative permittivity of the medium. The factor of 2 accounts for the round-trip travel of the pulse.

Given a 60.5 GHz carrier frequency (f_{RF}), the corresponding wavelength (λ) is approximately 5 mm. Thus, a 5 mm shift in the wavelet corresponds to a 2.5 mm target movement due to the round-trip path. This high frequency enables sub-millimeter movement detection, which is especially useful for applications such as vital sign monitoring.

The transmitted radar pulse $x(t)$ is modeled as:

$$x(t) = A(t) \cdot \cos(2\pi f_0 t + \theta) = \Re\left\{A(t)e^{j\theta}e^{j2\pi f_0 t}\right\} \tag{9}$$

where the envelope $A(t)$ is given by:

$$A(t) = \exp\left(-\frac{t^2}{2\tau^2}\right) \tag{10}$$

here, $A_0(t)$ is the delayed received envelope. The received signal undergoes a time delay of $\Delta T = \frac{2R_0}{c}$ and a phase shift of $\Delta\theta = -\frac{4\pi R_0}{\lambda}$, due to the propagation distance.

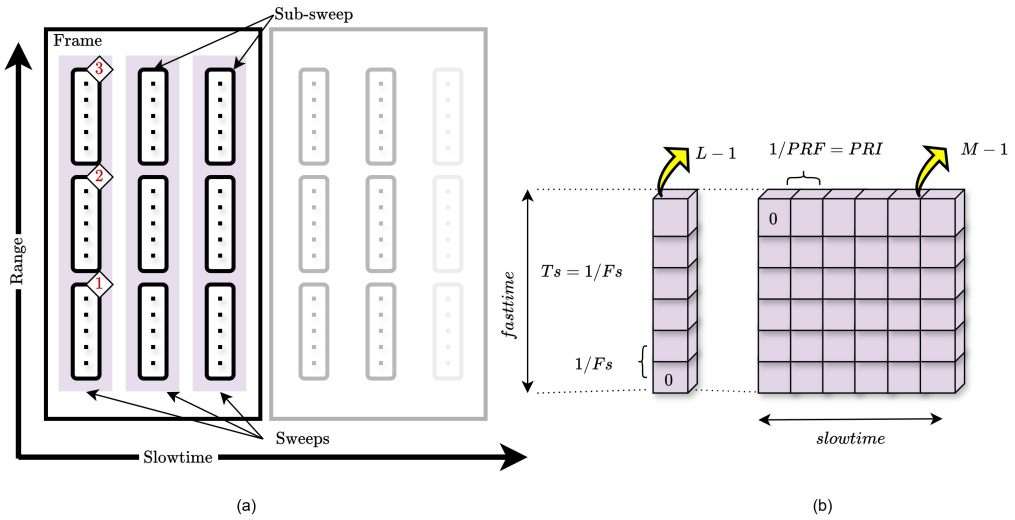

Figure 5: Radar data acquisition hierarchy (a) Sub-sweeps are grouped into sweeps and frames, where each sweep captures range information across bins; (b) Fast-time (range) and slow-time (temporal) samples into a 2D matrix representation.

B.2 Data Interpretation

As part of the signal model (Section 2.1) and the basis for target detection (Section 2.2), the raw radar data is represented as an IQ matrix where each element is a complex number corresponding to a specific sweep and range bin. For a radar system, the IQ data matrix consisting of magnitude and phase information with S sweeps per frame and D range bins per sweep is expressed as:

$$\text{Magnitude} = \sqrt{I[s,d]^2 + Q[s,d]^2}, \quad \text{Phase} = \tan^{-1}\left(\frac{Q[s,d]}{I[s,d]}\right) \tag{11}$$

The Sparse IQ service of the Acconeer Exploration Tool SDK organizes the radar data into a hierarchical structure consisting of frames and sweeps. Each frame contains multiple sweeps, where each sweep comprises several measurement points spanning the configured sensing range (as illustrated in Figure 5). The sweeps are sampled consecutively with a time interval T_s between the corresponding measurement points in consecutive sweeps. The sweep rate is defined as $f_s = 1/T_s$, while the frame rate is given by $f_f = 1/T_f$, where T_f is the frame period. To ensure that all sweeps are completed before the next frame starts, the following constraint must be satisfied:

$$T_f \geq N_s \cdot T_s \quad \Leftrightarrow \quad f_f \leq \frac{f_s}{N_s} \tag{12}$$

Subsweeps represent subregions within individual sweeps and allow for finer control of resolution and signal-to-noise ratio (SNR). To ensure a consistent SNR across sweeps, overlapping range configurations with different measurement profiles are used. In order to nullify the weakening of signals at a distance, subsweeps are used with increasing HWAAS (Hardware Averaging per Sample) and higher-resolution profiles. Each subsweep is configured with a start point, number of measured points, and step length, while each frame is formed by stacking constituent sweeps.

B.3 Phase Extraction

This section provides the detailed derivation for the method introduced in Section 2.3. The phase extraction algorithm begins with downsampling the IQ data matrix in the fast time dimension (range) and applies a low-pass filter in the slow time dimension (sweep). The filtered signal is expressed as:

$$\bar{x}[s,d] = \alpha_{\text{iq}}\bar{x}[s-1,d^*] + (1-\alpha_{\text{iq}})x_D[s,d^*] \tag{13}$$

where $\mathbf{x}_D[s,d^*]$ is defined as

$$x_D[s,d^*] = x\Big[s,\, dD + \frac{D}{2}\Big]. \tag{14}$$

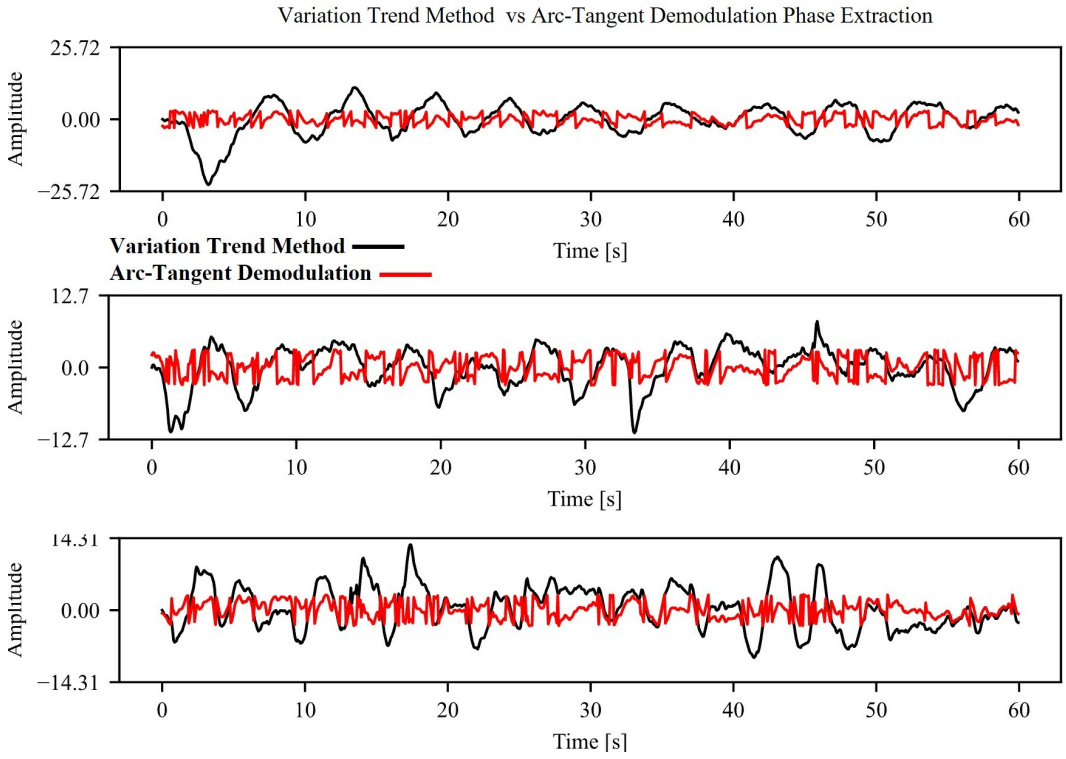

Figure 6: Phase extraction from three radar signals acquired in outdoor conditions using two methods: variation trend (black) and arctangent demodulation (red). The arctangent method requires extra steps like phase unwrapping, filtering, and baseline trend correction to align with the variation trend results.

α_{iq} is the low-pass filter coefficient defined as:

$$\alpha_{\text{iq}} = \exp\left(-\frac{2}{\tau_{\text{iq}} f_s}\right) \tag{15}$$

here, τ_{iq} is the time constant and f_s is the sweep (slow-time) rate. This filtering smoothens the signal while preserving the respiratory motion components. Then we compute the instantaneous phase iteratively using:

$$\phi[s] = \alpha_\phi \phi[s-1] + \angle\left\{\sum_{d-\Delta}^{d+\Delta} \bar{x}_D[s, d']\, \bar{x}_D^*[s-1, d']\right\} \tag{16}$$

where α_ϕ is the high-pass filter coefficient given by:

$$\alpha_\phi = \exp\left(-\frac{2 f_{\text{low}}}{f_s}\right) \tag{17}$$

In this expression, $\angle z$ denotes the phase angle of the complex number z, the superscript * represents the complex conjugate, and N_d is the number of samples per sweep after downsampling. This formulation captures the phase difference between consecutive sweeps, providing a single phase value $\phi[s]$ for each sweep that encodes a respiratory-induced displacement. The final phase signal is obtained through recursive summation of instantaneous phase changes across sweeps, resulting in a continuous output phase free from discontinuities and eliminating the need for explicit phase unwrapping. As shown in Figure 6, the variation trend approach (black curves) is compared against arctangent demodulation (red curves), where the phase is computed as $\tan^{-1}\left(\frac{Q[s,d]}{I[s,d]}\right)$, with $Q[s, d]$ and $I[s, d]$ representing the quadrature and in-phase components, respectively. The arctangent method requires additional computational steps such as phase unwrapping and baseline correction. This comparison highlights how the variation trend method offers a computationally efficient and robust alternative for phase extraction in radar-based respiratory monitoring.

C Proposed Method

C.1 DMD-t Tracking

DMD-t offers improved interpretability of real breathing dynamics compared to STFT-based tracking as illustrated in Fig. 7. Unlike STFT, it provides higher frequency resolution and greater stability, enabling reliable estimation of respiratory rate variability, crucial for clinical distress analysis and can be extended to heart rate variability monitoring. To validate practical applicability across diverse

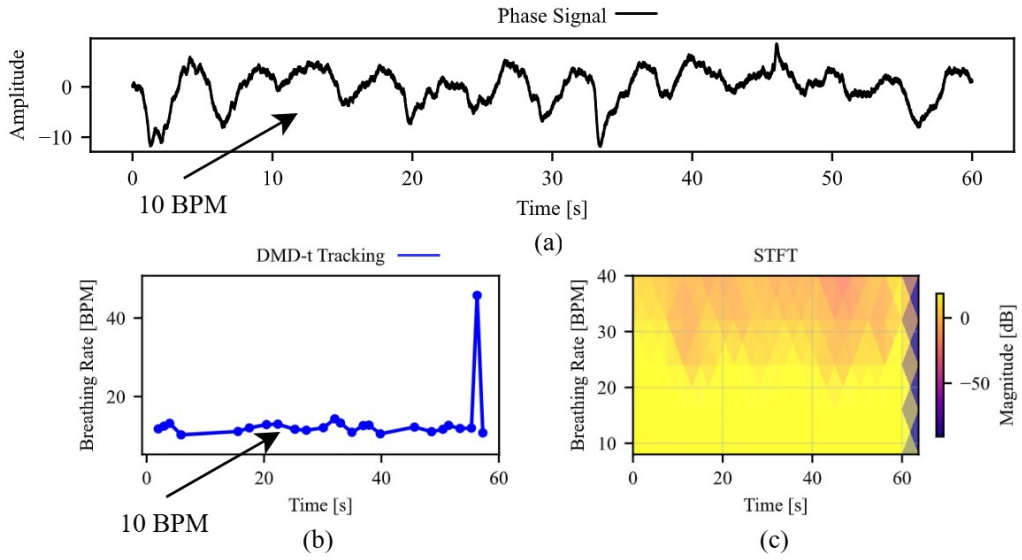

Figure 7: Phase analysis of a real radar signal. (a) Measured phase data; (b) DMD-t tracking effectively highlights phase dynamics; (c) STFT spectrogram offers lower clarity and resolution.

physiological conditions, we apply DMD-t to all 24 indoor participants' radar data. Figure 10 presents time-frequency spectrograms, where blue curves represent extracted instantaneous respiratory rates and color intensity indicates spectral energy concentration. It employs overlapping sliding windows to ensure continuous tracking across temporal segments. The full algorithmic pipeline is shown in (Fig. 9) from IQ service data to phase extraction, HDMD and Tracking..

Most participants (P1-P5, P7-P11, P14, P16-P23) exhibit stable breathing patterns characterized by concentrated spectral energy along the tracked trajectory. The narrow frequency bandwidth and consistent temporal evolution indicate regular respiratory cycles without significant motion artifacts. In contrast, participants P6, P12, P13, P15, and P24 present challenging scenarios with random body movements (RBM) during recording. These cases are characterized by broader frequency dispersion and intermittent high-energy bursts at non-respiratory frequencies corresponding to motion artifacts. Despite these challenges, DMD-t maintains tracking continuity by distinguishing between respiratory variations and transient motion interference. The varied spectral patterns across participants underscore the importance of adaptive tracking methods for real-world deployment.

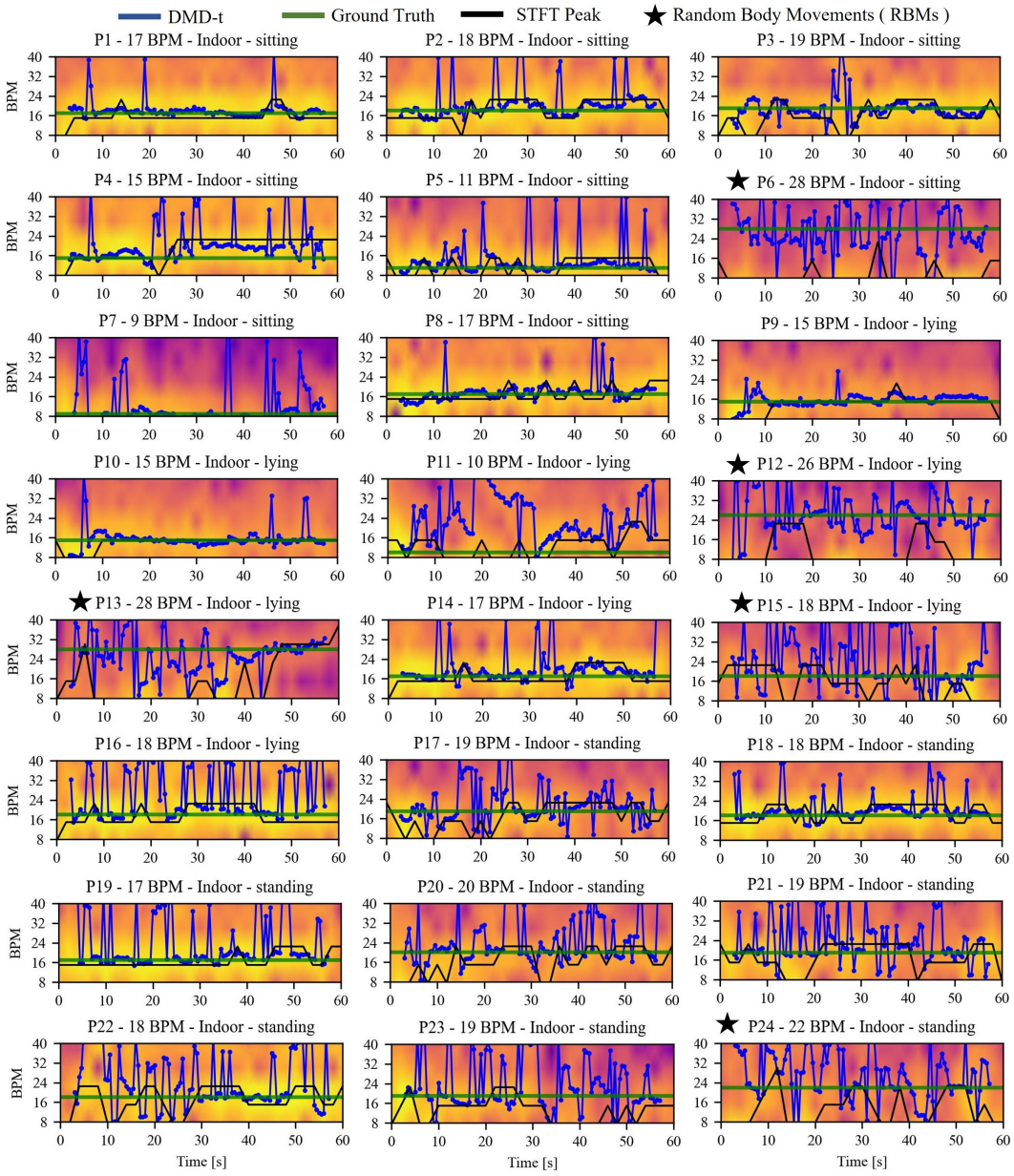

Figure 8: DMD-t respiratory tracking for 24 indoor participants. Each subplot shows the instantaneous respiratory rate (blue curve) over the DMD-t spectrogram, where color intensity indicates spectral energy concentration. Participants P6, P12, P13, P15, and P24 show random body movements (RBMs), while others exhibit stable breathing cycles.

Algorithm: Phase Extraction → HDMD → DMD-t Tracking

Input: $\mathsf{IQ}(s,d),\ \mathrm{fs}_{orig},\ T_{orig},\ \mathrm{fs},\ T,\ \tau_{iq},\ f_{low},\ D,\ m,\ r,\ W,\ S$

Output: $\phi(t),$ HDMD modes/frequencies, $\widehat{x}_{breath},$ DMD-t frequency track

1. Preprocessing / Range-bin Selection:

Compute $\mathrm{fs}_{orig} = N_{orig}/T_{orig};$ form complex IQ if needed.

$\overline{mag}(r) = \mathrm{mean}_t|\mathsf{IQ}|;\ r_{peak} = \arg\max_r \overline{mag}(r);$

$R = [r_{peak} - \Delta_r, \ldots, r_{peak} + \Delta_r].$

2. Temporal Filtering / Downsampling:

$\alpha_{iq} = e^{-2/(\tau_{iq}\mathrm{fs}_{orig})};\ \mathsf{filt}[:,:,t] = \alpha_{iq}\mathsf{filt}[:,:,t-1] + (1-\alpha_{iq})\mathsf{IQ}[:,:,t];$

Downsample range indices by factor D.

3. Phase Extraction (Variation Trend):

$\alpha_\phi = e^{-2f_{low}/\mathrm{fs}_{orig}};\ z_t = \sum_{a,r} \mathsf{filt}[a,r,t]\overline{\mathsf{filt}[a,r,t-1]};$

$\phi_{orig}[t] = \alpha_\phi \phi_{orig}[t-1] + \angle(z_t).$

4. Resampling:

Interpolate $\phi(t)$ from ϕ_{orig} to desired fs, $T.$

5. Hankel Matrix Construction:

$H_{i,j} = \phi[i+j-1];\ X = H[:, 1:n-1],\ Y = H[:, 2:n].$

6. Hankel DMD (HDMD):

$X = U\Sigma V^*;\ \widetilde{A} = U_r^* Y V_r \Sigma_r^{-1};\ \widetilde{A}W = W\Lambda;$

$\Phi = Y V_r \Sigma_r^{-1} W;\ f_i = \Im[\log(\lambda_i)/(2\pi\Delta t)];$

Keep modes with $0.1 \le |f_i| < 0.8$ Hz.

7. Breathing Reconstruction:

$b = \Phi_{\mathcal{S}}^{\dagger} X[:,1];\ \widetilde{X}_{dmd} = \Re\{\Phi_{\mathcal{S}} e^{\omega_{\mathcal{S}} t}\};$

$\widehat{x}_{breath} = \mathrm{DiagonalAverage}(\widetilde{X}_{dmd}).$

8. DMD-t Tracking:

For each window w (size $W,$ step S) :

H_w from $\phi(t);\ (\Phi_w, \Lambda_w, f_w) = \mathrm{HDMD}(H_w);$

Select dominant mode in $0.1{-}0.8$ Hz; $\hat{f}_w = |f_{w,i^*}|.$

Return: $\phi(t),\ (\Phi, \Lambda, f, \alpha),\ \widehat{x}_{breath},\ (\mathcal{T}, \hat{\mathcal{F}}, \hat{\mathcal{A}}).$

Figure 9: Hankel-DMD algorithm with DMD-t tracking

C.2 Phase Reconstruction

HDMD effectively removes residual harmonics, producing a smooth signal where peaks are clearly resolved as shown in Fig. 10(b). In contrast, EEMD struggles with mode mixing, leaving harmonics at inhalation and exhalation points that lead to frequency estimation errors and poor temporal resolution (Fig. 10(c)). VMD reconstruction depends heavily on mode selection and fails to suppress high-frequency noise, causing amplitude mismatches that prevent clear respiratory waveform isolation (Fig. 10(d)). While Wavelet Transform yields a cleaner reconstruction with reduced noise, residual harmonics remain and closely spaced peaks often merge, leading to ambiguity in respiratory pattern identification (Fig. 10(e)).

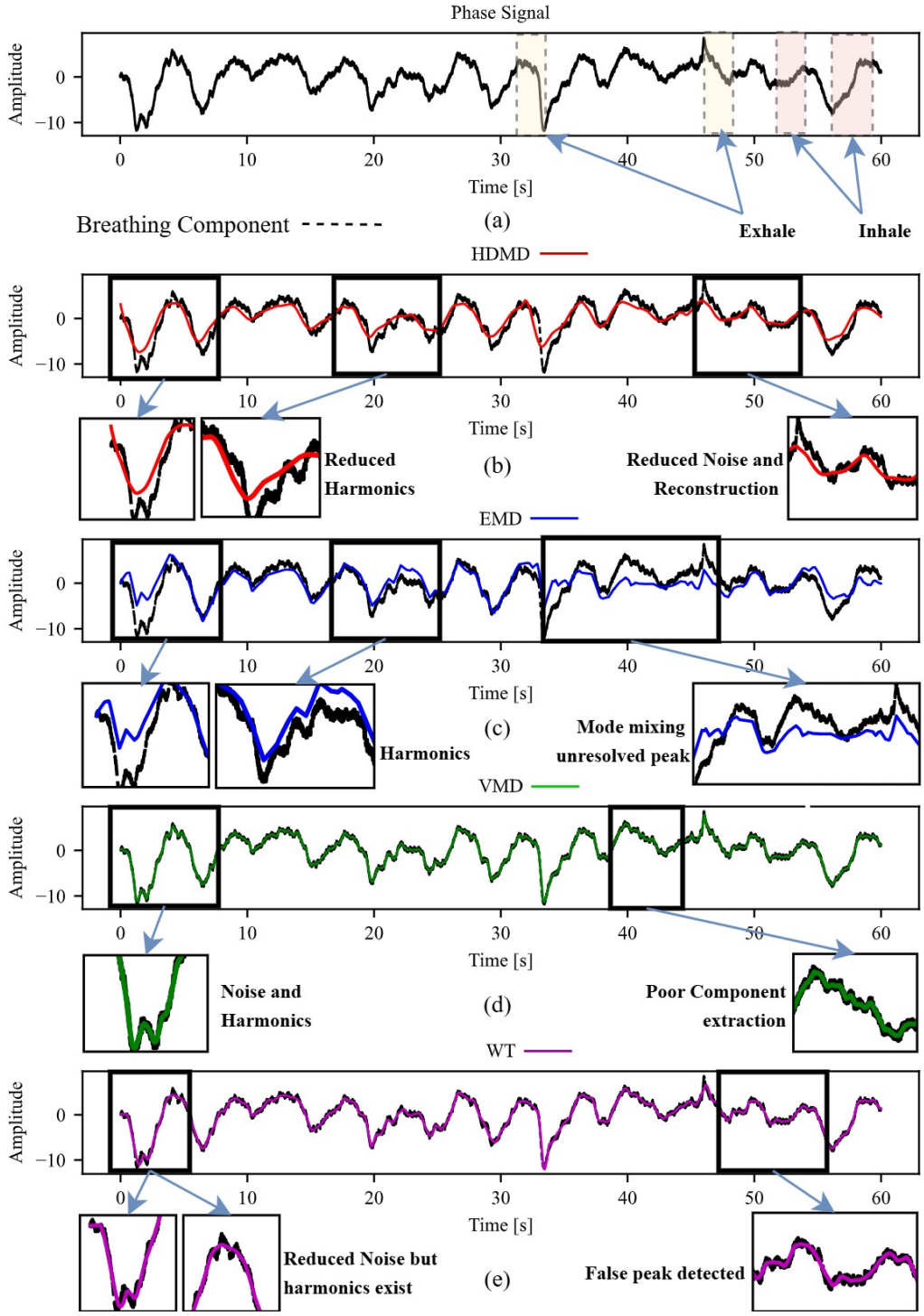

Figure 10: Phase reconstruction and analysis of a real radar signal. (a) Original signal phase; (b–e) phase reconstructions using HDMD, EEMD, VMD, and DWT, respectively. The methods track phase variations, with mismatches and reconstruction errors highlighted in affected time intervals.

D Experimental Setup

D.1 Hardware Configuration and Radar Platform

The experimental evaluation utilizes the Acconeer XM125 module integrating the A121 pulsed coherent mmWave radar, operating at 60.5 GHz, configured as a single-channel system with one transmitter and one receiver. The module is optimized for high precision, low power applications with inherent robustness against environmental interferences including ambient lighting, acoustic noise, and atmospheric particulates.

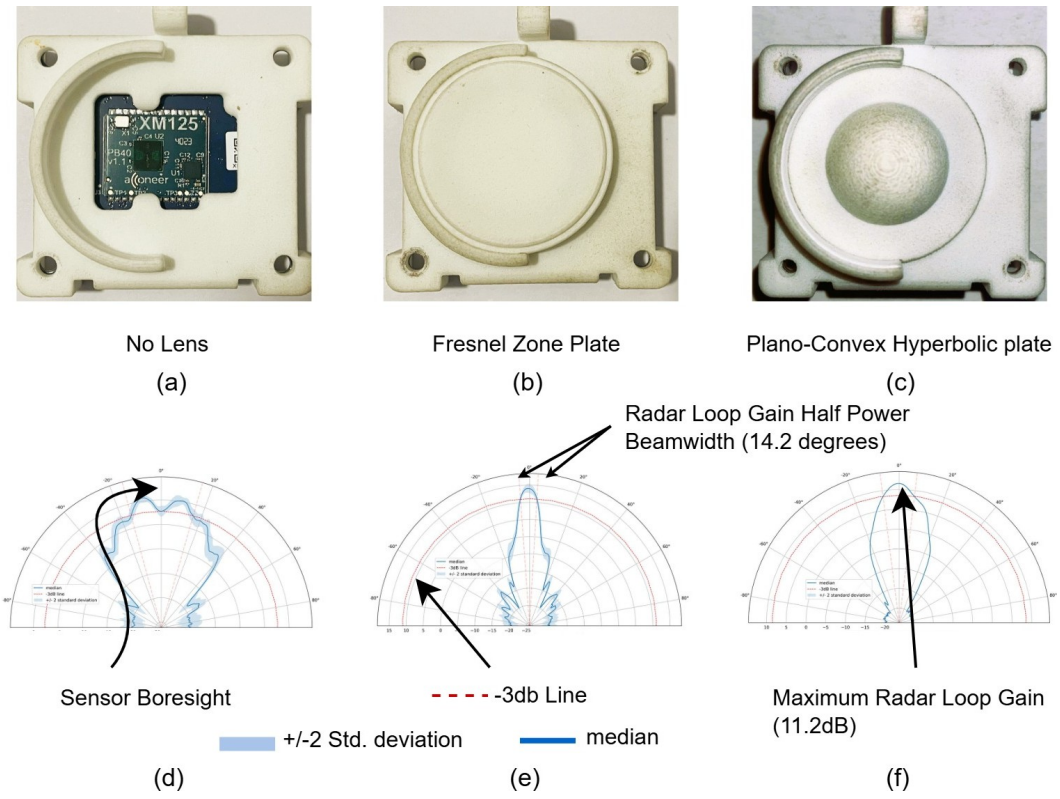

Figure 11: Comparison of beam patterns for the XM125 radar with different lens configurations. Top: (a) No lens, (b) Fresnel Zone Plate lens, (c) Plano-convex hyperbolic lens. Bottom: Corresponding radiation patterns showing beamwidth narrowing and gain enhancement with lens-assisted focusing.

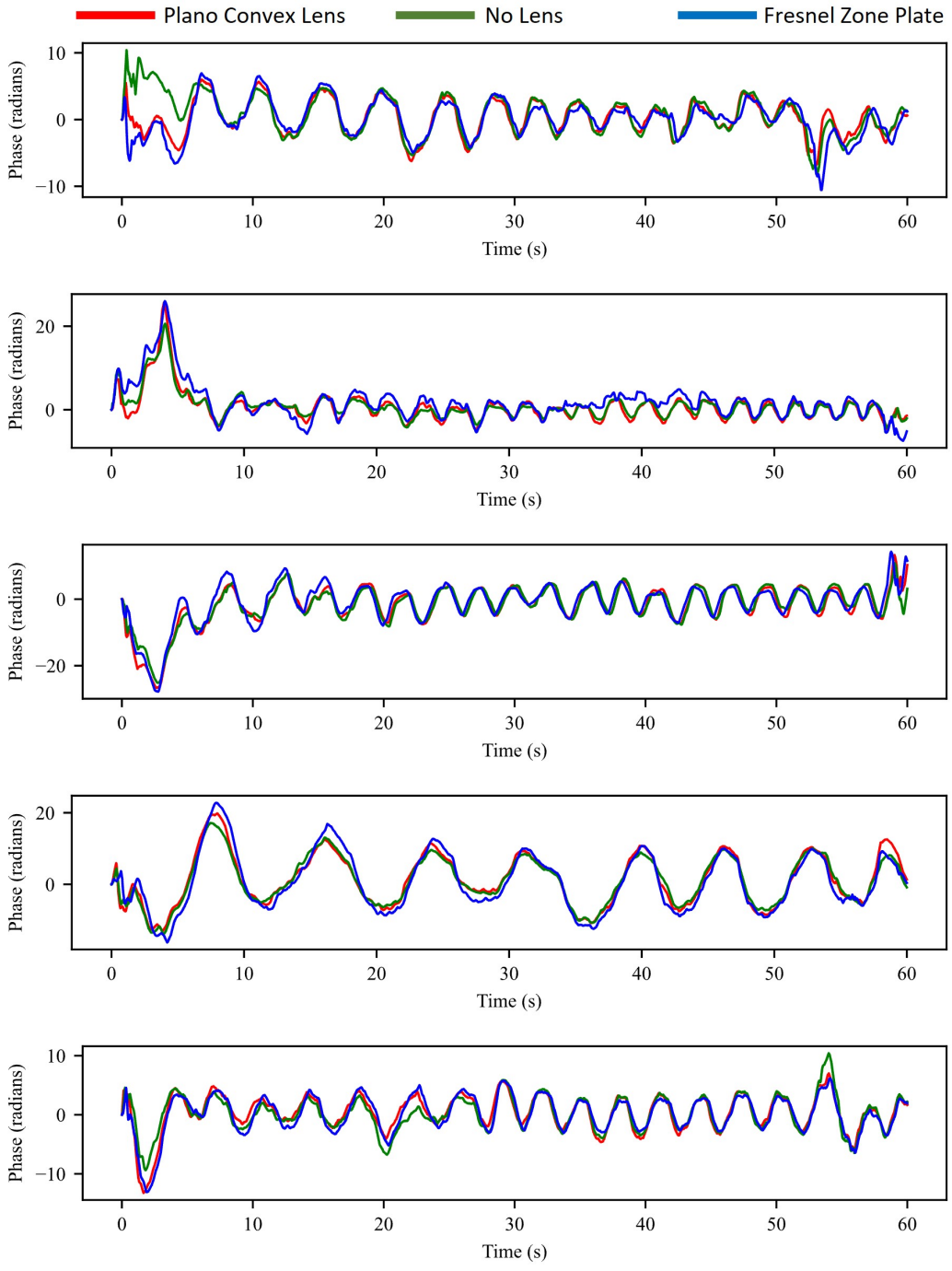

Figure 12: Phase signal comparison across different lens configurations. Red: Plano-convex lens; Blue: Fresnel Zone Plate (FZP); Green: No lens. The plano-convex lens yields smoother, higher-SNR phase trajectories with clearer respiratory cycles.

To enhance respiratory signal acquisition, we systematically evaluated three antenna configurations: bare radar module, plano-convex dielectric lens, and Fresnel Zone Plate (FZP) lens. The plano-convex lens from Acconeer's standard lens kit features a planar inner surface and convex outer surface designed for 60.5 GHz operation with material permittivity $\varepsilon_r \approx 2.6$ and focal distance $F = 10$ mm, achieving optimal F/D ratio ($\approx$ 0.5-0.8) for directivity and clutter rejection. The FZP lens operates on diffraction principles with concentric phase-correcting rings, offering thickness independence from diameter. The bare module exhibits broader beam patterns ($\sim$60° beamwidth) compared to the focused lens configurations ($\sim$20° beamwidth), making it more susceptible to environmental clutter and multipath interference. Table 3 presents respiratory rate estimation across all three configurations. The plano-convex lens achieved best performance with RMSE of 0.89 BPM, representing 53% improvement over no-lens (1.88 BPM) and 23% improvement over FZP (1.15 BPM). Figure 12 illustrates representative phase signals, where the plano-convex lens produces consistently cleaner waveforms with higher SNR and distinct respiratory cycles, while the no-lens configuration shows increased noise and baseline drift. The lens was mounted on a height-adjustable tripod maintaining 1.5-2m distance from the subject's chest area across different postures.

Table 3: Comparison of breathing rate estimation (in BPM) under different lens configurations.

Person ID	**Actual Rate (BPM)**	**Measured Rate (BPM)**		
	Ground Truth	**No Lens**	**Fresnel Zone Plate Lens**	**Plano-Convex Lens**
P1	24	24.42	23.43	23.16
P2	23	24.14	24.10	24.17
P3	19	19.23	19.41	19.16
P4	20	20.34	20.42	19.96
P5	15	13.69	12.90	15.59
P6	12	11.87	12.25	12.07
P7	16	15.99	16.11	15.11
P8	20	20.12	20.54	20.05
P9	24	24.73	24.12	24.25
P10	22	20.48	22.82	21.18
P11	15	17.52	17.88	16.49
P12	21	21.64	21.21	20.69
P13	20	19.79	19.90	19.21
P14	8	7.75	7.91	7.93
P15	18	18.45	18.26	17.75
P16	19	19.57	19.32	19.56
P17	16	17.47	15.38	15.08
P18	18	17.74	18.17	17.82
P19	19	11.03	16.16	16.81
P20	19	17.41	17.96	18.12
P21	20	20.48	19.61	19.70
P22	20	21.35	21.97	21.54
P23	23	22.96	21.43	21.86
P24	24	24.79	23.67	22.70
RMSE (BPM)		1.88	1.15	**0.89**

D.2 Radar Configuration Parameters

The Acconeer XM125 radar system is configured for remote respiratory monitoring using the Sparse IQ service. Operating at a maximum sweep rate of 2575 Hz, the system achieves frame rates up to 411.8 Hz, providing dense temporal sampling for phase extraction and respiratory signal analysis (target range: 0.15–0.5 Hz or 9–30 BPM). The sensing range spans 0.225–1.525 m with 20 mm spatial resolution (start point: 80, 40 range bins, step length: 8), enabling robust subject localization across typical monitoring distances. Signal quality is enhanced through coherent amplitude processing (Profile 3), 16 dB receiver gain, and 8-fold hardware averaging per sample (HWAAS). Real-time IQ data acquisition utilizes the Acconeer Exploration Tool SDK (v4.9.0+) with USB streaming at 40 samples per frame.

D.3 Data Collection

Data collection includes both controlled indoor and outdoor environments to evaluate algorithm robustness. The study involves 24 participants (12 male, 12 female, aged 20-60 years) across six experimental conditions combining three postures (sitting, lying, standing) with two environmental settings (indoor/outdoor). Indoor environments provide controlled conditions with minimal electromagnetic interference and stable lighting for baseline performance validation. Outdoor scenarios introduce realistic challenges, including environmental interference, wind-induced movement, variable conditions, and ground clutter reflections.

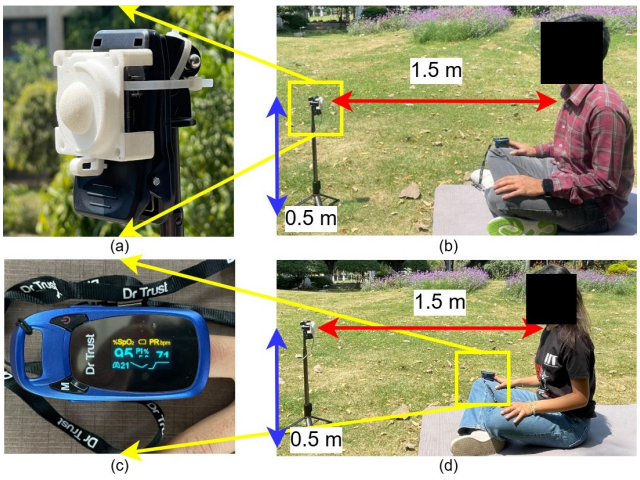

Figure 13: Outdoor Data collection (a) XM125 radar module. (b, d) The experimental configuration, showing the sensor placed 1.5 m from the subject. (c) Pulse oximeter used for ground truth validation.

Each subject undergoes timed recording sessions across all six conditions. Ground truth respiratory rates were recorded using a clinical-grade capnography system (BM-K12, Bird Meditech) and a portable fingertip pulse oximeter (Dr. Trust). The capnograph has an accuracy of ± 1 breath or $\pm 10\%$, while the oximeter estimates respiratory rate from photoplethysmography (PPG) with a rated accuracy of ± 1 BPM.

To assess the reliability of the oximeter-based ground truth used in outdoor experiments, simultaneous recordings from both devices were obtained for 24 indoor subjects. The oximeter readings showed an RMSE of 0.74 BPM (3.87% NRMSE) relative to capnography. These results confirm that the portable oximeter provides sufficiently accurate reference data for outdoor validation, with measurement uncertainty comparable to our radar estimation error (RMSE 0.55 BPM).

E Baseline Methods and Metrics

E.1 Baseline Algorithms

E.1.1 Ensemble Empirical Mode Decomposition (EEMD)

EEMD decomposes a signal into a finite set of Intrinsic Mode Functions (IMFs) through an iterative sifting process. For a given signal $x(t)$, the decomposition is expressed as:

$$x(t) = \sum_{i=1}^{N} c_i(t) + r_N(t) \tag{18}$$

where $c_i(t)$ represents the i-th IMF and $r_N(t)$ is the residual component. Each IMF satisfies two conditions: (1) the number of extrema and zero-crossings must differ by at most one, and (2) the mean of the upper and lower envelopes is zero at all points. The sifting process for obtaining the k-th IMF involves:

$$h_{1k}(t) = x(t) - m_1(t) \tag{19}$$

where $m_1(t)$ is the mean of upper and lower envelopes formed by cubic spline interpolation of local maxima and minima.

E.1.2 Variational Mode Decomposition (VMD)

VMD formulates the decomposition as a constrained variational problem. It seeks K modes $\{u_k\}$ and their corresponding center frequencies $\{\omega_k\}$ by solving:

$$\min_{\{u_k\},\{\omega_k\}} \left\{ \sum_{k=1}^{K} \left\| \partial_t \left[\left(\delta(t) + \frac{j}{\pi t} \right) * u_k(t) \right] e^{-j\omega_k t} \right\|_2^2 \right\} \tag{20}$$

subject to $\sum_{k=1}^{K} u_k = f$, where $\delta(t)$ is the Dirac delta function, $*$ denotes convolution, and j is the imaginary unit. The solution is obtained using the Augmented Lagrangian method:

$$u_k^{n+1}(\omega) = \frac{\hat{f}(\omega) - \sum_{i \neq k} \hat{u}_i(\omega) + \frac{\hat{\lambda}(\omega)}{2}}{1 + 2\alpha(\omega - \omega_k)^2} \tag{21}$$

where $\hat{(\cdot)}$ denotes the Fourier transform and α is the balancing parameter.

E.1.3 Discrete Wavelet Transform (DWT)

The Discrete Wavelet Transform (DWT) of a signal $x(t)$ is defined as:

$$W(a,b) = \frac{1}{\sqrt{a}} \int_{-\infty}^{\infty} x(t) \psi^* \left(\frac{t-b}{a} \right) dt \tag{22}$$

where $\psi(t)$ is the mother wavelet, a is the scale parameter, b is the translation parameter, and $*$ denotes complex conjugate. For the Discrete Wavelet Transform (DWT), the signal is decomposed into approximation coefficients A_j and detail coefficients D_j at level j:

$$A_j[k] = \sum_n x[n] \phi_{j,k}[n] \tag{23}$$

$$D_j[k] = \sum_n x[n] \psi_{j,k}[n] \tag{24}$$

where $\phi_{j,k}[n]$ and $\psi_{j,k}[n]$ are the scaling and wavelet functions, respectively.

E.1.4 Wavelet Cosine Transform (WCT)

WCT combines wavelet decomposition with cosine transform. After wavelet decomposition, each subband is further processed using the Discrete Cosine Transform (DCT):

$$X_k = \sum_{n=0}^{N-1} x_n \cos \left[\frac{\pi}{N} \left(n + \frac{1}{2} \right) k \right], \quad k = 0, 1, \ldots, N-1 \tag{25}$$

The WCT coefficient for subband s and frequency index k is:

$$\text{WCT}(s,k) = \text{DCT}(\text{DWT}_s(x)) \tag{26}$$

where $\text{DWT}_s(x)$ represents the wavelet coefficients in subband s.

E.1.5 Band-Pass Filtering (BPF)

BPF isolates frequency components within a specified range $[\omega_1, \omega_2]$. For an ideal band-pass filter, the frequency response is:

$$H(\omega) = \begin{cases} 1, & \omega_1 \leq |\omega| \leq \omega_2 \\ 0, & \text{otherwise} \end{cases} \tag{27}$$

In practice, a Butterworth band-pass filter of order n is commonly used:

$$|H(\omega)|^2 = \frac{1}{1 + \left(\frac{\omega^2 - \omega_0^2}{\omega \cdot BW} \right)^{2n}} \tag{28}$$

where $\omega_0 = \sqrt{\omega_1 \omega_2}$ is the center frequency and $BW = \omega_2 - \omega_1$ is the bandwidth.

E.1.6 Moving Average (MAV)

The simple moving average of window size N is defined as:

$$\bar{x}[n] = \frac{1}{N} \sum_{k=0}^{N-1} x[n-k] \tag{29}$$

The exponential moving average with smoothing factor α is:

$$\bar{x}[n] = \alpha x[n] + (1-\alpha)\bar{x}[n-1] \tag{30}$$

where $0 < \alpha \leq 1$. The weighted moving average assigns different weights w_k to different samples:

$$\bar{x}[n] = \frac{\sum_{k=0}^{N-1} w_k x[n-k]}{\sum_{k=0}^{N-1} w_k} \tag{31}$$

E.1.7 Compressed Sensing with Orthogonal Matching Pursuit (CS-OMP)

CS-OMP reconstructs sparse signals from compressed measurements. Given measurements $\mathbf{y} = \mathbf{\Phi x} + \mathbf{n}$, where $\mathbf{\Phi} \in \mathbb{R}^{M \times N}$ is the measurement matrix and $\mathbf{n}$ is noise, OMP iteratively selects columns of the sensing dictionary $\mathbf{\Psi}$:

$$\Lambda^{(k)} = \Lambda^{(k-1)} \cup \{\arg\max_j |\langle \mathbf{r}^{(k-1)}, \boldsymbol{\psi}_j \rangle|\} \tag{32}$$

$$\hat{\mathbf{x}}_{\Lambda^{(k)}} = \arg\min_{\mathbf{z}} \|\mathbf{y} - \mathbf{\Phi\Psi}_{\Lambda^{(k)}} \mathbf{z}\|_2^2 \tag{33}$$

$$\mathbf{r}^{(k)} = \mathbf{y} - \mathbf{\Phi\Psi}_{\Lambda^{(k)}} \hat{\mathbf{x}}_{\Lambda^{(k)}} \tag{34}$$

where $\Lambda^{(k)}$ is the support set at iteration k, $\mathbf{r}^{(k)}$ is the residual, and $\boldsymbol{\psi}_j$ are the dictionary atoms.

E.1.8 Finite Impulse Response (FIR) Filtering

An FIR filter of length N is characterized by its impulse response $h[n]$:

$$y[n] = \sum_{k=0}^{N-1} h[k] x[n-k] \tag{35}$$

The frequency response is:

$$H(\omega) = \sum_{k=0}^{N-1} h[k] e^{-j\omega k} \tag{36}$$

For linear phase FIR filters, the coefficients satisfy symmetry conditions. The Parks-McClellan algorithm designs optimal FIR filters by minimizing the maximum error in the passband and stopband:

$$E(\omega) = W(\omega)[H_d(\omega) - H(\omega)] \tag{37}$$

where $H_d(\omega)$ is the desired frequency response and $W(\omega)$ is the weighting function.

E.2 Evaluation Metrics

E.2.1 Pearson Correlation Coefficient (PCC)

The PCC measures the linear correlation between the original signal $\mathbf{x}$ and reconstructed signal $\hat{\mathbf{x}}$:

$$\text{PCC} = \frac{\sum_{i=1}^{N}(x_i - \bar{x})(\hat{x}_i - \bar{\hat{x}})}{\sqrt{\sum_{i=1}^{N}(x_i - \bar{x})^2}\sqrt{\sum_{i=1}^{N}(\hat{x}_i - \bar{\hat{x}})^2}} \tag{38}$$

where $\bar{x}$ and $\bar{\hat{x}}$ are the sample means of the original and reconstructed signals, respectively. PCC ranges from -1 to 1, where:

- PCC = 1: Perfect positive linear correlation (ideal waveform preservation)
- PCC = 0: No linear correlation
- PCC = -1: Perfect negative linear correlation

This metric evaluates how well the temporal morphology and phase relationships of the respiratory waveform are preserved after decomposition and reconstruction.

E.2.2 Mean Squared Error (MSE)

MSE quantifies the average squared differences between original and reconstructed signals:

$$\text{MSE} = \frac{1}{N}\sum_{i=1}^{N}(x_i - \hat{x}_i)^2 \tag{39}$$

where N is the number of samples. MSE provides a measure of reconstruction fidelity, with lower values indicating better performance. MSE is sensitive to outliers and gives higher weight to larger errors, making it suitable for detecting significant reconstruction artifacts.

E.2.3 Root Mean Squared Error (RMSE)

RMSE is the square root of MSE, providing error magnitude in the same units as the original signal:

$$\text{RMSE} = \sqrt{\frac{1}{N}\sum_{i=1}^{N}(x_i - \hat{x}_i)^2} \tag{40}$$

RMSE offers better interpretability than MSE as it represents the standard deviation of prediction errors. For respiratory signals, RMSE directly indicates the average amplitude deviation in the original signal units.

E.2.4 Normalized Root Mean Squared Error (NRMSE)

NRMSE normalizes RMSE by the signal's dynamic range to enable comparison across different signal amplitudes:

$$\text{NRMSE} = \frac{\text{RMSE}}{\max(\mathbf{x}) - \min(\mathbf{x})} \times 100\% \tag{41}$$

Alternative normalizations include division by the mean or standard deviation:

$$\text{NRMSE}_{\text{mean}} = \frac{\text{RMSE}}{|\bar{x}|} \times 100\% \tag{42}$$

$$\text{NRMSE}_{\text{std}} = \frac{\text{RMSE}}{\sigma_x} \times 100\% \tag{43}$$

where σ_x is the standard deviation of the original signal. NRMSE enables fair comparison between signals with different amplitude ranges and provides a percentage-based error metric.

E.2.5 Respiratory Rate Estimation Accuracy

For respiratory rate estimation, we evaluate the accuracy of extracted breathing frequency f_r compared to the ground truth $f_{r,\text{gt}}$:

Absolute Error:

$$\text{AE} = |f_r - f_{r,\text{gt}}| \tag{44}$$

Relative Error:

$$\text{RE} = \frac{|f_r - f_{r,\text{gt}}|}{f_{r,\text{gt}}} \times 100\% \tag{45}$$

Mean Absolute Error (MAE):

$$\text{MAE} = \frac{1}{M}\sum_{j=1}^{M}|f_{r,j} - f_{r,\text{gt},j}| \tag{46}$$

where M is the number of test segments.

Mean Absolute Percentage Error (MAPE):

$$\text{MAPE} = \frac{1}{M}\sum_{j=1}^{M}\frac{|f_{r,j} - f_{r,\text{gt},j}|}{f_{r,\text{gt},j}} \times 100\% \tag{47}$$

F Extended Results

F.1 Ablation Studies

Effect of Sampling Frequency Variations: Sampling frequency f_s determines data density critical for SVD-based Hankel-DMD, where matrix dimensions strongly depend on available samples. To evaluate this effect, the constructed respiratory signal was resampled at different f_s values and reconstructed using HDMD, EEMD, VMD, and Wavelet Transform (Table 1). At higher sampling frequencies (240 Hz), HDMD consistently achieved the best correlation with the ground truth, accurately capturing variability while effectively suppressing high-frequency flutter (0.16 MSE, 0.994 PCC). In contrast, EEMD suffers from escalated mode mixing producing distorted oscillations (2.42 MSE, 0.899 PCC), VMD shows amplitude mismatches despite maintaining high correlation (1.85 MSE, 0.993 PCC), while Wavelet Transform provides competitive results but introduces overshoots from residual harmonics (1.15 MSE, 0.953 PCC). At lower sampling frequencies (100 Hz), data sparsity degraded HDMD performance (1.26 MSE, 0.958 PCC), leading to mode mixing and pronounced amplitude mismatches due to limitations in Hankel matrix construction. Wavelet Transform also performed poorly (2.56 MSE, 0.892 PCC), showing increased frequency mismatches and less smooth reconstructions. VMD, however, demonstrated relative robustness under sparse data, achieving higher correlation (0.989 PCC) despite increased MSE (3.62), though it still failed to fully suppress high-frequency noise and harmonics. Overall, HDMD exhibits strong dependence on adequate sampling density, while VMD shows greater resilience under reduced sampling.

Effect of Signal Duration and Embedding Length: The variation in performance of algorithms based on signal duration is shown in Table 1. HDMD is inherently dependent on the Hankel embedding parameter m, which represents the number of rows in the matrix. For longer signals (180s), richer embeddings ($m \approx 300$–500) yield smooth reconstructions (0.54 MSE, 0.985 PCC at 120s vs. 0.64 MSE, 0.980 PCC at 180s) with accurate amplitude and frequency representations. In comparison, EEMD exhibits significant degradation at longer duration (MSE increases from 1.68 to 3.92), suffering from harmonic leakage, mode mixing, and amplitude-frequency mismatches. Wavelet Transform achieves the lowest MSE at longer duration (0.63) but with reduced correlation (0.975), while VMD maintains higher correlation (0.983) with increased MSE (0.73), remaining sensitive to parameter tuning and unable to fully suppress higher-order harmonics. For shorter durations (120s), HDMD maintains stable mode isolation as the Hankel matrix construction in HDMD provides adequate temporal embedding when sufficient matrix rows are maintained ($m \geq f_s/f_{\min}$). VMD reconstructions show consistent performance across durations, EEMD continues to suffer from high-frequency flutter and harmonic contamination, and Wavelet Transform introduces overshooting, peak shifting, and baseline offsets.

Reconstruction Performance Under Gaussian Noise: In Table 1 HDMD shows minimal effect from Gaussian noise on breathing component reconstruction, achieving near-perfect reconstruction at low noise levels ($k = 0.5$: 0.006 MSE, 1.000 PCC) and maintaining high accuracy under elevated noise ($k = 3$: 0.54 MSE, 0.985 PCC). EEMD exhibits counterintuitive behavior where reconstruction quality improves with increased noise. While MSE increases from 3.64 to 4.68, the correlation slightly improves from 0.801 to 0.731, reflecting stochastic resonance effects where controlled noise perturbations aid in separating intrinsic mode functions that remain poorly distinguished in overly smooth signals. VMD maintains stable performance with a slight increase in MSE ($0.93 \rightarrow 1.72$) showing good noise resilience. Wavelet Transform shows consistent behavior across noise conditions ($0.969 \rightarrow 0.958$ PCC) with minor performance degradation. HDMD, however, consistently provides smooth reconstructions with minimal noise impact, aside from a slight amplitude mismatch at higher levels of white Gaussian noise.

F.2 Computational Complexity

Based on the computational analysis of signal decomposition methods applied to a 120-second signal sampled at 300 Hz , clear runtime differences were observed aligned with their algorithmic complexities. Discrete Wavelet Transform (DWT) was the fastest, completing in 4 ms with linear $\mathcal{O}(n)$ complexity. VMD and EEMD required 0.86 s and 38.9 s respectively, consistent with $\mathcal{O}(K \cdot n \cdot \log n)$ and $\mathcal{O}(k \cdot n^2)$ complexities, where K and k denote the number of modes and intrinsic mode functions. Hankel Dynamic Mode Decomposition (HDMD) was the slowest at 5.4 s, approximately $6.3\times$ longer

than VMD, reflecting its $\mathcal{O}(n^2)$ to $\mathcal{O}(n^3)$ complexity arising from singular value decomposition (SVD) operations on the Hankel matrix.

As a data-driven method, HDMD requires higher sampling rates to construct effective Hankel embeddings. Denser sampling provides more temporal information for robust subspace identification and respiratory component reconstruction. This requirement directly impacts computational cost, as the Hankel matrix dimensions scale with the number of samples. However, this computational investment enables superior frequency resolution and harmonic suppression capabilities. In contrast, while DWT and VMD offer significantly faster processing with satisfactory frequency resolution, they fail to adequately denoise, remove harmonics, and maintain accuracy under random body movements, as demonstrated in Table 2. For fair comparison, all methods were evaluated on identical signal lengths.

While HDMD offers excellent frequency resolution and robust breathing signal extraction even in challenging conditions, its computational cost remains a key limitation for real-time deployment or extended signal durations without algorithmic optimization or hardware acceleration. Additionally, HDMD performance degrades under sparse sampling due to insufficient Hankel embedding structure and, though less sensitive than VMD, still requires careful tuning of the embedding dimension parameter.

G Conclusion and Limitations

This work establishes Hankel Dynamic Mode Decomposition as a robust framework for radar-based respiratory monitoring, achieving superior performance (3.14% NRMSE) compared to traditional decomposition methods across diverse environmental conditions. While HDMD demonstrates exceptional signal reconstruction quality and noise resilience through its Koopman operator-based approach, the method faces practical limitations including computational complexity ($\mathcal{O}(n^2)$ to $\mathcal{O}(n^3)$) that restricts real-time deployment, sensitivity to sparse sampling conditions below 60 Hz, and current evaluation scope limited to single-person scenarios. The DMD-t tracking extension successfully enables analysis of non-stationary respiratory dynamics, providing enhanced temporal resolution compared to traditional spectral methods. Future research directions should focus on algorithmic optimization for real-time implementation, extension to multi-person tracking scenarios using HDMD, and integration with edge computing platforms while maintaining the superior frequency resolution that makes HDMD particularly suitable for privacy-preserving, contactless physiological monitoring in clinical and mobile health applications.